Low dispersion finite volume/element discretization of the enhanced Green-Naghdi equations for wave propagation, breaking and runup on unstructured meshes

M. Kazolea[a], A. G. Filippini[b], M. Ricchiuto[a]

[a]*INRIA, Univ. Bordeaux, CNRS, Bordeaux INP, IMB, UMR 5251, 200 Avenue de la Vieille Tour, 33405 Talence cedex, France*
[b]*BRGM French Geological Survey, Coastal Risk and Climate Change 3 Av. C. Guillermin 45060 Orleans Cedex 2, France*

Abstract

We study a hybrid approach combining a FV and FE method to solve a fully nonlinear and weakly-dispersive depth averaged wave propagation model. The FV method is used to solve the underlying hyperbolic shallow water system, while a standard P^1 finite element method is used to solve the elliptic system associated to the dispersive correction. We study the impact of several numerical aspects: the impact of the reconstruction used in the hyperbolic phase; the representation of the FV data in the FE method used in the elliptic phase and their impact on the theoretical accuracy of the method; the well-posedness of the overall method. For the first element we proposed a systematic implementation of an iterative reconstruction providing on arbitrary meshes up to third order solutions, full second order first derivatives, as well as a consistent approximation of the second derivatives. These properties are exploited to improve the assembly of the elliptic solver, showing dramatic improvement of the finale accuracy, if the FV representation is correctly accounted for. Concerning the elliptic step, the original problem is usually better suited for an approximation in $H(\text{div})$ spaces. However, it has been shown that perturbed problems involving similar operators with a small Laplace perturbation are well behaved in H^1. We show, based on both heuristic and strong numerical evidence, that numerical dissipation plays a major role in stabilizing the coupled method, and not only providing convergent results, but also providing the expected convergence rates. Finally, the full mode, coupling a wave breaking closure previously developed by the authors, is thoroughly tested on standard benchmarks using unstructured grids with sizes comparable or coarser than those usually proposed in literature.

Keywords: Green-Naghdi equations, hybrid scheme, Finite Volumes, Finite Elements, high order, wave breaking

Email addresses: `maria.kazolea@inria.fr` (M. Kazolea), `a.filippini@brgm.fr` (A. G. Filippini), `mario.ricchiuto@inria.fr` (M. Ricchiuto)

Contents

1. Introduction

Accurate simulations of water wave's propagation and non-linear wave transformations is of fundamental importance to marine and coastal engineering. Over the last decades, significant efforts in the development of depth averaged models have been made in order to provide the means of accurately predicting near-shore wave processes.

One of the most applied depth averaged models is the Non-linear Shallow Water Equations (NSWE).They are applied to describe long wave hydrodynamics when the vertical acceleration of water particles can be neglected assuming the flow to be nearly horizontal. They are able to model important aspects of wave propagation phenomena, the general characteristics of the run-up process, and the wave breaking with broken waves represented as shocks. However they are not appropriate for deeper waters and shoaling since they neglect all the dispersive effects that play a very important role. Taking dispersive effects in to account is of critical importance if we want to study the nearshore wave propagation and transformation. The main tool for performing studies including also dispersion have been pioneered by Boussinesq [12], who derived a system of equations under the assumption that non-linearity and disperion are week and in the same order of magnitude. Peregrine [59] was the first to derive a Boussinesq-type (BT) system of equations with topography terms. During the 1990s researchers focused on improving the dispersive properties of the original model of Peregrine and push the range of validity of the equations towards deeper waters, leading mainly to BT models restricted to situations with weakly non-linear interactions. Some famous models among them are [56, 50, 6]. However in many practical applications the effects of the non-linearity are too large to be treated using weakly non-linear BT models. Green and Naghdi [32] derived a fully non-linear weakly dispersive model (GN model) which gained a lot of attention the last two decades. The range of validity of this last model requires only the dispersion parameter to be small, but it does not impose any restriction to the non-linearity. However, linear dispersion properties of the GN model are the same as those of Peregrine. In

3

[18] and [11] an enhanced model with an improved dispersion relationship is proposed. This model is used in our work.

For the numerical discretization of the GN equations in 1DH all the common techniques like Finite Elements (FE), Finite Volumes(FV) and Finite Differences (FD) have been used, see for example [31, 18, 11, 55] and references therein. In less studied two horizontal dimensions (2D) cases, and only in Cartesian meshes, the numerical techniques that have been used are again FD [24, 77, 79], combinations of FV and FD methods [61, 69, 46] and Discontinuous Galerkin (DG) methods [47]. Up to the authors knowledge, the only works on general unstructured meshes are [26], where a new form of the GN equations is solved using a DG method, and the very recent work of [51], where a combined Hybridizable Discontinus Galerkin and Runge-Kutta DG formulation is used for the same set of equations. In this work we extended the idea presented by the authors in [31] and [29]. We solve the enhanced GN equations, first introduced in [45], using a flexible combination of FV and the standard C^0 Galerkin FE method on unstructured meshes. We would like to stress that the methodology discussed in the paper can be applied to other dispersive free surface models using a similar formulation in which a dispersive source is added to the shallow water equations, and independent discretizations are written for the hyperbolic component and for the dispersive forcing. See for example [71, 17] for some examples.

The manuscript is organized as follows. In section 2 we present the model equations while in section 3 we describe the solution strategy which we follow in this work. Section 4 presents a higher order solver for the hyperbolic part of the equations, i.e the shallow water equations and the next section shows how to incorporate the elliptic part in to the system using the FE technique. A discussion on the well-posedness of the coupled method is following while section 7 presents a time-continues dispersion error analysis. Section 8 is devoted to implementation details and finally in section 9 the numerical results justify and verify our choices. The paper is concluded by a discussion and outlook on future work.

2. The fully-nonlinear/weakly-dispersive model

In this work we use the enhanced GN (eGN) system of equations in the form proposed in [10]. This formulation provides an order $O(\mu)$ depth averaged approximation of the nonlinear wave equations, being μ the dispersion parameter defined as $\mu = h_0^2/\lambda^2$, where h_0 is the reference water depth and λ the wavelength. The two dimensional form of the system can be written in the following form:

$$h_t + \nabla \cdot (h\mathbf{u}) \;=\; 0 \tag{1}$$

$$(I + \alpha T)\left(\mathbf{q}_t + \nabla \cdot \left(\frac{\mathbf{q} \otimes \mathbf{q}}{h}\right) + gh\nabla\eta\right) + \frac{g}{\alpha}h\nabla\eta + hQ(\mathbf{u}) \;=\; 0$$

where the operators $T(\cdot)$ and $Q(\cdot)$ are:

$$T(\cdot) \;=\; -\frac{1}{3}\nabla\left(h^3\nabla \cdot \frac{(\cdot)}{h}\right) - \frac{h^2}{2}\left(\nabla \cdot \frac{(\cdot)}{h}\right)\nabla b + \frac{1}{2}\nabla\left(h^2\nabla b \cdot \frac{(\cdot)}{h}\right) + h\left(\nabla b \cdot \frac{(\cdot)}{h}\right)\nabla b, \tag{2}$$

$$Q(\cdot) \;=\; \frac{2}{3h}\nabla\left(h^3\left(\nabla(\cdot)_1 \cdot \nabla^\perp(\cdot)_2 + (\nabla \cdot (\cdot))^2\right)\right) + h^2\left(\nabla(\cdot)_1 \cdot \nabla^\perp(\cdot)_2 + (\nabla \cdot (\cdot))^2\right)\nabla b + $$

$$+ \;\; \frac{1}{2h}\nabla\left(h^2\left((\cdot) \cdot \left((\cdot) \cdot \nabla\right)\nabla b\right)\right) + \left((\cdot) \cdot \left((\cdot) \cdot \nabla\right)\nabla b\right)\nabla b. \tag{3}$$

We denote $h(\mathbf{x}, t) = h_0 + \eta(\mathbf{x}, t) - b(\mathbf{x})$ the total water depth, where $\eta(\mathbf{x}, t)$ the free surface elevation with respect to the water rest state h_0, $b(\mathbf{x})$ the topography variation and $\mathbf{u}(\mathbf{x}, t) = (u, v)$ the flow velocity as shown in figure 1. $(\cdot)_1$ and $(\cdot)_2$ indicates respectively the first and second component of the vector $(\cdot)$ and $\nabla^\perp$ states for the normal gradient operator.
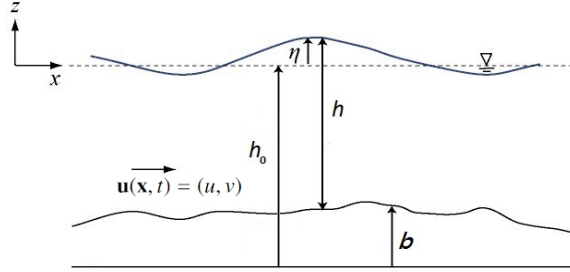

Figure 1: Description of the free surface flow problem and main notation.

The operator $T(\cdot)$ plays a key role, as its inversion is necessary to be able to obtain evolution equations for the physical variables. $T(\cdot)$ can be written in compact form involving two operators $S_1(\cdot)$, $S_2(\cdot)$ and their adjoints $S_1^\star(\cdot)$, $S_2^\star(\cdot)$, as:

$$T(\cdot) = S_1^\star\left(hS_1\left(\frac{(\cdot)}{h}\right)\right) + S_2^\star\left(hS_2\left(\frac{(\cdot)}{h}\right)\right) \tag{4}$$

where

$$S_1(\cdot) = \frac{h}{\sqrt{3}}\nabla \cdot (\cdot) - \frac{\sqrt{3}}{2}\nabla b \cdot (\cdot), \quad S_2 = \frac{1}{2}\nabla b \cdot (\cdot). \tag{5}$$

Note that this formulation is essential to show the coercivity of the operator $(I + \alpha T)$, see [31] and referenced therein for further details. In the above expressions α is a parameter which is used to improve the dispersion properties of the model in order to be close to the those of the full Euler equations. The interested reader cen be refereed to [44] . Note also that when $\alpha = 1$ we retrieve the original GN equations.

The linear dispersion and shoaling properties of the fully nonlinear GN and eGN models are comparable to those of the weakly nonlinear models of Peregrine and Madsen and Sorensen respectively, extensively described in [29]. On the other hand, the nonlinear shoaling properties of a weakly/strongly nonlinear model is not easy to be examined analytically. As discussed in [29], one way to test the nonlinear shoaling properties of a model is by performing the test of Grilli et al. [33]. The test consists of a solitary wave with relative amplitude $\alpha/h_0 = 0.2m$, propagating on a water depth of $0.44m$ and shoaling on to a constant slope of $1 : 35$. Ten wave gauges have been placed along the flume to measure the free surface elevation. All of them are placed before the breaking point with the last one being the closest to the breaking point. Figure 2 compares the experimental wave's envelope with the result performed by four weakly non-linear models: Peregrine (P) [59], Abbott (A) [1], Madsen and Sorensen (MS) [50] and the MSP system. The last one is a modified system of Peregrine's equations written in a wave amplitude-velocity form, see [29, 30] for further details. In this work, we performed the same test on the fully nonlinear GN and eGN models and we added the computed results on the figure. Our result has been obtained using the discretization method presented in this work and it is a grid convergent solution, such that the plotted curve can be seen as genuine representations of the behaviour of the model. We can observe that as soon as the nonlinear effects dominate (this happens close the breaking region) the phenomenon is better reproduced by the fully nonlinear models and even better by the eGN equations used in this work.

3. Solution strategy and geometrical notation

To numerically solve (1), we rewrite the system of two dimensional enhanced GN equations as:

$$h_t + \nabla \cdot \mathbf{q} = 0, \tag{6}$$

$$\mathbf{q}_t + \nabla \cdot \left(\frac{\mathbf{q} \otimes \mathbf{q}}{h} \right) + gh\nabla\eta = \boldsymbol{\Phi} \tag{7}$$

$$(I + \alpha T)\,\boldsymbol{\Psi} = W - R, \tag{8}$$

$$\boldsymbol{\Phi} = \boldsymbol{\Psi} + \frac{gh}{\alpha}\nabla\eta \tag{9}$$

by splitting the original system in its elliptic and hyperbolic parts, through the definition of the new variable $\boldsymbol{\Phi} = [\phi_x, \phi_y]^T$. $\boldsymbol{\Phi}$ accounts for the dispersive effects and has the role of a non-hydrostatic pressure gradient
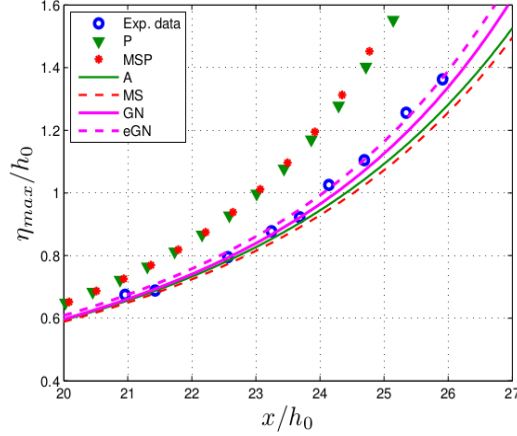
6

Figure 2: Wave envelope on the 9 gauges along the domain. Comparison between different weakly nonlinear models, GN, eGN and the experimental data. A-Abbot model, P-Peregrin model, MS-Madsen and Sorensen, MSP-Madsen and Sorensen in velocity form.

in the Shallow water equations. We define

$$
\begin{aligned}
W &= -\frac{gh}{\alpha}\nabla\eta \\
R &= hQ\left(\frac{\mathbf{q}}{h}\right)
\end{aligned}
\tag{10}
$$

where the operators $T(\cdot)$ and $Q(\cdot)$ are (2) and (3) respectively. In this work we solve (6)-(9) using a hybrid Finite Element (FE)- Finite volume (FV) scheme where the elliptic part of the system is discretized by means of the continuous Galerkin FE method. The hyperbolic part of the system is discretized by the two dimensional formulation of the finite volume scheme inspired by the works [41, 42]. We refer to the work [41], which has been proven to be a robust scheme, capable of simulating wave transformations providing accurate results in complex scenarios and over two dimensional unstructured triangular meshes.

So we consider a triangulation of the spatial domain which we denote by Ω_h, with the roman h denoting the largest element diameter. In the approach developed here, we will both make use of elements defined by each of the non-overlapping triangles of the mesh, as well as of a *median-dual* partition in oder to generate non-overlapping nodal control volumes. Let us denote by K the generic triangular element, and by K_i the set of elements sharing node i. We then denote by C_i the median dual cell obtained by joining the gravity centers of the triangles in K_i with the midpoints of the edges meeting in i. Simple geometry shows that $|C_i| = \sum_{K \in K_i} \frac{|K|}{3}$. We also define D_i as the set of nodes connected to i. For any $j \in D_i$, the shared portion

7

of boundary of C_i and C_j is named ∂C_{ij}, and it is composed by the union of two segments connecting the barycenters of the two triangles sharing the edge ij with the edge midpoint (see figure 3). The boundary of the median dual cell of i can thus be defined as: $\partial C_i = \sum_{j \in K_i} \partial C_{ij}$. Moreover, we define $\mathbf{r}_{ij}$ the vector connecting nodes i and j Note finally, that the intersection of C_i intersects each element $K \in K_i$ can be split into two half cells associated to the two edges stemming from i. The half cell containing node j is denoted by C_{ij}^K, and we set $C_{ij} = \bigcup_{K \in K_i \cap K_j} C_{ij}^K$ so that $C_i = \bigcup_{j \in D_i} C_{ij}$.

4. Hyperbolic step: third order FV scheme and derivatives recovery via successive corrections

For simplicity we rewrite the system of conservation laws (6)-(7) as

$$\mathbf{U}_t + \nabla \cdot \mathbf{F}(\mathbf{U}) = \mathbf{S}_b + \mathbf{\Phi}_i. \tag{11}$$

with $\mathbf{U} = [h, \ \mathbf{q}]^T$, $\mathbf{F} = [\mathbf{q}, \ \mathbf{q} \otimes \mathbf{q}/h + gh^2 \mathbf{I}_2]^T$, with $\mathbf{I}_2$ the rank 2 identity matrix, and with $\mathbf{S}_b = -[0, \ gh\nabla b]^T$. The FV integration over each computational cell C_i leads to the semi-discrete form of the scheme as:

$$\frac{\partial \overline{\mathbf{U}}_i}{\partial t} + \frac{1}{|C_i|} \sum_{j \in D_i} \int_{\partial C_{ij}} \hat{\mathbf{F}} \cdot \mathbf{n} = \frac{1}{|C_i|} \sum_{j \in D_i} \int_{C_{ij}} \mathbf{S}_b + \overline{\mathbf{\Phi}}_i \ , \tag{12}$$

where $\overline{\mathbf{U}}_i$ is the volume averaged value of $\mathbf{U}$ over C_i, $\mathbf{n}$ is the unitary outward vector normal to ∂C_i, and with $\overline{\mathbf{\Phi}}_i = \int_{C_i} \mathbf{\Phi}$ evaluated using numerical quadrature (cf. section §5). In the above expression, $\hat{\mathbf{F}}$ is the numerical flux defined here using the approximate Riemann solver of [66]. The method used here is relatively standard and we will not provide much details. It is based on a well balanced formulation of the integrals of the fluxes and of the bathymetry source, as well as a robust modification of the reconstruction and numerical flux to cope with the wet/dry transition. We refer the interested reader to e.g. [8, 15, 16], and to [41, 43] for some details on our implementation.

To reach high-order spatial accuracy, we have to reconstruct each component of the physical variables and bed topography. Following the classical strategy by [76] (cf also [69, 41] and [31]), to reduce the introduction of spurious numerical dispersion we avoid second order approximations for the hyperbolic terms, and look into the design of a fully third order method. This is achieved in this paper by means of a successive correction method which iteratively improves derivatives computed by means of the standard Green-Gauss formula. This allows to construct k-exact polynomials with all local operations, requiring only the exchange of information between adjacent cells. In particular for a third order method we need a quadratic polynomial requiring the knowledge of gradient and Hessian of the variables in the dual cell. The

8

standard Green-Gauss formula is unfortunately not well suited for general unstructured meshes on which it provides first order derivatives which are at most consitent (1st order accurate), and second derivatives which may event be inconsistent. There are many methods to overcome this: from the classical least square method used in k-exact method by Barth in [4, 2, 3], to more recent ones used in [73, 74, 80] and [19]. The basic limitation most of the above methods is the computational cost, related to the need of solving a more or less large linear system, and the complexity of the implementation, related to the need of assembling and using an enlarged stencil.

We follow here the method first proposed by [13, 37, 36] and more recently in [60]. In the references the authors constructed a generalized hybridization of Green-Gauss and Least square methods, called quasi-Green method, which results in a first-order accurate gradient on unstructured meshes. A successive correction method allows the construction of consistent gradient and Hessian on unstructured meshes. The idea of the corrections is to impose exact consistency with the monomials of appropriate degree. A thorough discussion and the general derivation of the method can be found in [60, 53] to which we refer for details. All the above works are using cell centered methods. In our work we have extended the approach to node centered finite volumes. Very recently (and independently on this work) [68] and [67] also provided a similar re-formulation for the linear advection equation and of the incompressible Euler equations.

In our work, we develop a node centered successive correction method for the hyperbolic nonlinear shallow water system, and appropriately combine it with a slope limiter to handle bores and hydraulic jumps. To our knowledge this is the first time that a nodal variant of the successive reconstruction technique is used for a hyperbolic system and combined with a limiter. We recall hereafer the basic steps to obtain a third order reconstruction. Most of the formulas allowing the implementation are provided in an appendix.

4.1. Polynomial expansion and derivative reconstruction via successive corrections

The reconstruction problem consists in defining a piece-wise polynomial of degree k that approximates $f(\mathbf{x})$ to the $(k + 1)^{\text{th}}$ order of accuracy. Our aim is to calculate approximations of the solution to the faces of the cells. To do this, we use high order polynomials obtained by Taylor expansions. Let us introduce the vector and tensor moments

$$\begin{aligned} \delta^{(1)}_{G_i}(\mathbf{x}) &= (\mathbf{x} - \mathbf{x}_{G_i}) \,, \\ \delta^{(2)}_{G_i}(\mathbf{x}) &= \delta^{(1)}_{G_i} \otimes \delta^{(1)}_{G_i} = (\mathbf{x} - \mathbf{x}_{G_i}) \otimes (\mathbf{x} - \mathbf{x}_{G_i}) \end{aligned} \tag{13}$$

For a third order scheme ($k = 2$) a conservative approximation is of the form [5, 57]

$$f_i(\mathbf{x}) = \bar{f}|_{G_i} + \mathbf{D}^{(1)}_f|_{G_i} \cdot (\mathbf{x} - \mathbf{x}_{G_i}) + \frac{1}{2} \mathbf{D}^{(2)}_f|_{G_i} : \left(\delta^{(2)}_{G_i}(\mathbf{x}) - M^{(2)}_i \right), \tag{14}$$
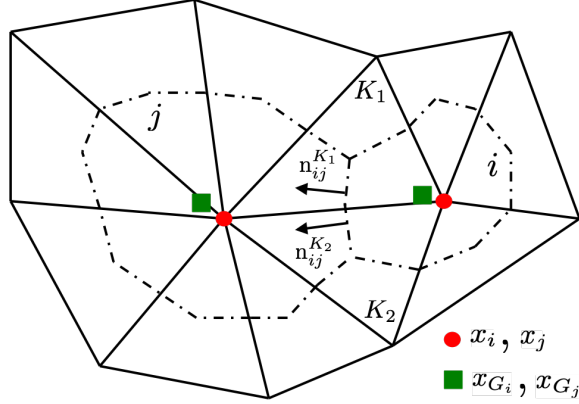
9

Figure 3: Notation and volume area used in the successive correction method

where where $\mathbf{D}_f^k|_{G_i}$ represents the order k spatial derivative of f (gradient, Hessian, etc) at the gravity center $\mathbf{x}_{G_i}$, and where the $A : B$ operator denotes the element by element lumped matrix product

$$A : B = \sum_{i,j} A_{ij} B_{ij} \,.$$

The matrix M_i contains the geometric moments:

$$M_i^{(2)} = \int_{C_i} \delta_{G_i}^{(2)}$$

Note that these geometric moments are mesh dependent quantities that can be pre-computed via numerical quadrature and stored (cf. Appendix A for mode details). The cell polynomials thus defined guarantee the conservation property

$$\frac{1}{|C_|i} \int_{C_i} f_i(\mathbf{x}) dS = \bar{f}|_{G_i}.$$

The crucial step is to computation of the spatial derivatives with the desired accuracy.

4.1.1. First derivatives

To get the first derivative at the gravity center of C_i, we apply the quasi-Green gradient approximation. This consists in a Green-Gauss reconstruction with a correction restoring the consistency of the operator on general meshes [53]. We end up with an operator approximating the gradient to first order accuracy on general meshes as (cf again figure 3 for the notation):

$$\mathbf{D}_f^{(1,o1)}|_{G_i} = M_1^{-1} \sum_{j \in D_i} \left[w_{ij}^{K_2} \bar{f}_i + (1 - w_{ij}^{K_1}) \bar{f}_j \right] \mathbf{n}_{ij}^{K_1}. \tag{15}$$

where the superscript $o1$ denotes that the approximation is first order accurate, and with the weights w_{ij} computed based on the relative distance of the cell center's $\mathbf{x}_i$ to its face:

$$w_{ij}^{K_1} = \frac{\mathbf{s}_{ij}^{K_1} \cdot \mathbf{n}_{ij}^{K_1}}{\mathbf{r}_{ij} \cdot \mathbf{n}_{ij}^{K_1}} , \quad \mathbf{s}_{ij}^{K_1} = \frac{1}{2}\mathbf{x}_G^{K_1} + \frac{1}{4}(\mathbf{x}_i + \mathbf{x}_j) \tag{16}$$

and similarly for $w_{ij}^{K_2}$. The 2×2 matrix $(M_1)_i$ corrects the gradient to ensure its consistency. It is computed by imposing that for $f = x$ we have $\mathbf{D}_x^{(1,o1)}|_{G_i} = (1,0)$, and similarly for $f = y$ we have $\mathbf{D}_y^{(1,o1)}|_{G_i} = (0,1)$. This leads to:

$$M_{1_i} = [\sum_{j \in D_i} w_{ij}^{K_1}(\mathbf{x}_{G_j} - \mathbf{x}_{G_i}) \otimes \mathbf{n}_{ij}^{K_1} + w_{ij}^{K_2}(\mathbf{x}_{G_j} - \mathbf{x}_{G_i}) \otimes \mathbf{n}_{ij}^{K_2}]^T \tag{17}$$

As the geometrical moments, this correction matrix is mesh dependent, but can be pre-computed and stored before the simulations. The first order gradient $\mathbf{D}_f^{(1,o1)}|_{G_i}$ allows to construct polynomials with second order of accuracy at most.

4.1.2. Second derivatives and second order corrected gradients

Once consistent first derivatives are available in all cells, we can proceed to a second iteration which will provide consistent second derivatives and improved gradients. As previously stated, a first order approximation of the second derivatives is enough to guarantee third order of accuracy for the overall polynomial (14). Unfortunately, unless the mesh presents special symmetries, applying (15) twice results in an inconsistent approximation of $\mathbf{D}_f^{(2)}|_{G_i}$. We denote hereafter this approximation as

$$\mathbf{D}_f^{(2,o0)}|_{G_i} = \mathbf{D}^{(1,o1)}(\mathbf{D}_f^{(1,o1)})|_{G_i}$$

The idea is to correct this quantity as done for the gradient

$$\mathbf{D}_f^{(2,o1)}|_{G_i} = M_{2_i}^{-1} \mathbf{D}_f^{(2,o0)}|_{G_i} = M_{2_i}^{-1} \mathbf{D}^{(1,o1)}(\mathbf{D}_f^{(1,o1)})|_{G_i} \tag{18}$$

As for the gradient, the correction matrix M_{2_i} can be computed component by component by requiring the approximation to be consistent when applied to $\mathbf{x} \otimes \mathbf{x}$, so that for example $(\mathbf{D}_{x^2}^{(2,o1)}|_{G_i})_{11} = 2$, $(\mathbf{D}_{y^2}^{(2,o1)}|_{G_i})_{22} = 2$, $(\mathbf{D}_{yx}^{(2,o1)}|_{G_i})_{12} = 1$, etc. It can be shown [35] that M_{2_i} ca be obtained by a double application of the first derivative of first order derivative to $(\mathbf{x} - \mathbf{x}_{G_i}) \otimes (\mathbf{x} - \mathbf{x}_{G_i})$. For brevity we omit here the expressions obtained, which are reported in detail in appendix A.

The computation of a first order accurate second order derivative is not enough to achieve third order accuracy in the reconstruction. We also have to correct the approximation of the first derivative for it to be

11

at least second order. To obtain a correction strategy, we can compare the Taylor series development of the exact gradient with the one obtained using the available reconstructed derivatives :

$$
\begin{aligned}
\nabla f^{\text{exact}} = \nabla f\big|_{G_i} & + \nabla(\nabla f)\big|_{G_i} \cdot (\mathbf{x} - \mathbf{x}_{G_i}) + O(\mathrm{h}^2) \\
= \mathbf{D}_x^{(1),(o1)}\big|_{G_i} + O(\mathrm{h}) & + \mathbf{D}_f^{(2),(o1)}\big|_{G_i} \cdot (\mathbf{x} - \mathbf{x}_{G_i}) + O(\mathrm{h}^2)
\end{aligned}
\tag{19}
$$

The first order remainder on the second line, is due to the poor accuracy of the available gradient. For the gradient to be second order the second line should provide an exact answer for $f = (\mathbf{x} - \mathbf{x}_{G_i}) \otimes (\mathbf{x} - \mathbf{x}_{G_i})$. This is precisely the strategy suggested in [53, 60] to correct the gradient. So in practice we set

$$
\mathbf{D}^{(1,o2)}\big|_{G_i} = \mathbf{D}^{(1,fo)}\big|_{G_i} + M_{1_i}^{o2}\mathbf{D}^{(2,o1)}\big|_{G_i} \;,
\tag{20}
$$

where $M_{1_i}^{o2}$ is obtained by requiring the errors in the second line of (19) to vanish when $f = (\mathbf{x} - \mathbf{x}_{G_i}) \otimes (\mathbf{x} - \mathbf{x}_{G_i})$. For our 2D case $M_{1_i}^{o2}$ is a 2×3 matrix of the form (full expressions available in appendix A):

$$
M_1^{o2} = -\begin{bmatrix}
(\alpha_i)_x - x_{G_i} & (\beta_i)_x & (\gamma_i)_x - y_{G_i} \\
(\alpha_i)_y & (\beta_i)_y - y_{G_i} & (\gamma_i)_y - x_{G_i}
\end{bmatrix}.
$$

Note that all of the above matrices are only involved in local operations (involving nearest neighbours), they can all be pre-computed and stored during a pre-proccesing step, and then used to update the gradients by simple matrix-vector multiplications. There is no need of solving multiple linear systems. These are the main advantages of this method.

Unfortunately, the correction matrices seem to have no theoretical property guaranteeing their invertibility. However in all the cases that we examined here and in the references using the same approach, no problem was ever observed even in quite irregular meshes. Another issue is how to preserve the accuracy near boundaries. In this paper we have been only concerned with two conditions: symmetry or periodic conditions along straight lines. In both cases we have used ghost cells. For the symmetry/slip wall conditions we have defined the ghost values on a locally mirrored mesh on which scalar quantities (depth and bathymetry) have been copied, and vectors rotated by 180° wrt normal. In this framework, third order of accuracy can be obtained easily only for straight boundaries for which two layers of elements are mirrored in order to have enough stencil to compute the successive correction derivatives. Periodic conditions are imposed simply by extending the connectivity of the mesh to include the correspondence of the periodic boundaries so that all the geometrical quantities, as well as the residuals account for periodicity.

4.1.3. Capturing of non-smooth solutions and limiting

In order to prevent oscillations from developing in the numerical solution we use the slope limiter proposed by Michalak and Ollivier-Gooch in [54], for higher order MUSCL numerical schemes on unstructured meshes using a cell centered fv scheme for the Euler equations. Following the spirit of the above work we write the limited form of the higher order reconstruction in the middle point M of an edge connecting the nodes i and j, as

$$f_i(\mathbf{x}_M) = \bar{f}|_{G_i} + Lim_M \left(\mathbf{D}_f^{(1)}|_{G_i} \cdot (\mathbf{x}_M - \mathbf{x}_{G_i}) + \frac{1}{2}\mathbf{D}_f^{(2)}|_{G_i} : \left(\delta_{G_i}^{(2)}(\mathbf{x}_M) - M_i^{(2)} \right) \right). \tag{21}$$

The design of the slope limiter requires three steps. First we have to find the minimum $(\delta f)_{min}^i$ and the maximum values $(\delta f)_{max}^i$ of the difference $\bar{f}|_{G_j} - \bar{f}|_{G_i}$. in the stencil formed by the cell i and all the direct neighbors j. Then we compute the unlimited reconstructed value $f(\mathbf{x})_M$ and finally we compute the maximum allowable value for Lim_i as:

$$Lim_M \quad = \quad \begin{cases} g\left((\delta f)_{min}^i\right) & \text{if } f(\mathbf{x})_M - \bar{f}_i > 0, \\ g\left((\delta f)_{max}^i\right) & \text{if } f(\mathbf{x})_M - \bar{f}_i < 0, \\ 1 & \text{if } f(\mathbf{x})_M - \bar{f}_i = 0 \end{cases} \tag{22}$$

where $g(x) = \frac{x^2+2x}{x^2+x+2}$.

4.2. Numerical verification for smooth and non-smooth flows

We provide here a quick verification of the hyperbolic step. First we consider the smooth travelling vortex solution proposed by [63], and widely used in literature to mesure the accuracy of discretizations for the shallow water equations. Please refer to [63] for the precise definition of the test. We compute the solution at finite time as prescribed in the reference on a series of regular and irregular unstructured grids. The reference size of the coarsest mesh is h = 0.107573, which is reduced to half at each refinement step. The convergence of the depth error is reported on figure 4. Following the discussion in section 4 we performed the test in both structured and unstructured meshes confirming that the Green-Gauss reconstruction on unstructured meshes, spoils the convergence since is not able to produce consisted gradients. The picture confirms that the nominal accuracy is measured in practice in third order case when the derivatives are recovered via the successive correction approach. For the second order case the Green-Gauss is consisted with the gradient so the order of convergence is 2 interdependently of the mesh. The results are omitted for brevity.

We then consider the Monai valley benchmark [49], a classical test inspired by a flume experiment reproducing a scaled down version of the 1993 the Hokkaido-Nansei-Oki tsunami impact on the Monai
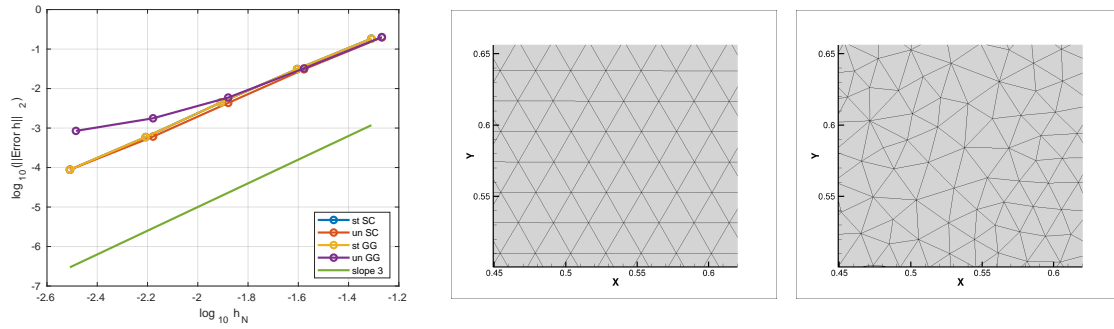
13

Figure 4: Error decay for the third order scheme. Representative structure and unstructure meshes.

valley. The test involves bore formation, propagation, and reflection, as well runup. Following [62], we have run the experiment on an unstructured grid adapted to the bathymetry variations, and we show the wave patterns obtained at time $16.5s$ (see figure 5) with the second and third order scheme, as well as the water height times series in two of the gauges of the experiment (figure 6).
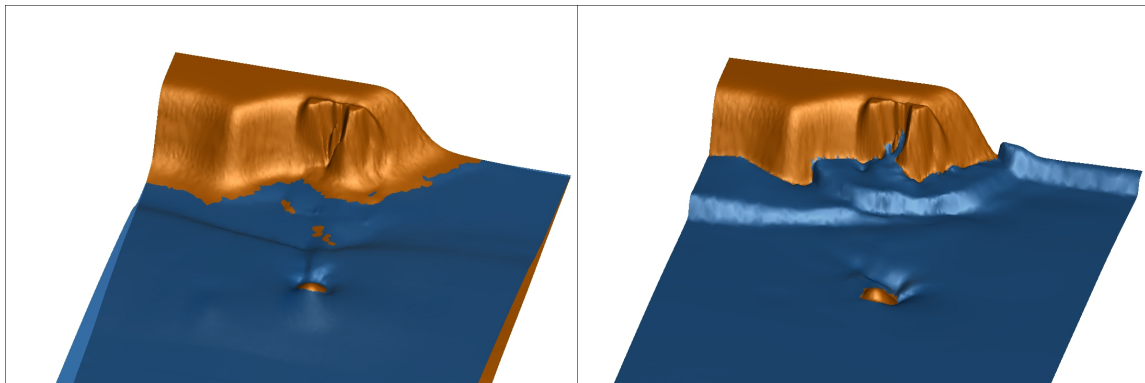

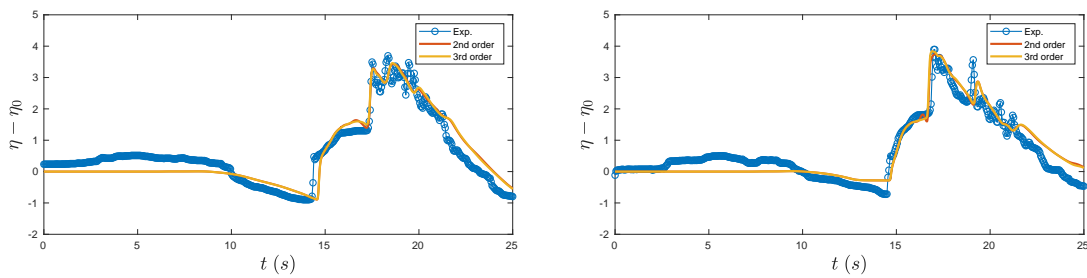Figure 5: Monai valley: 3d view at time t=14.5 and t=16.5 s using the third order scheme.

Figure 6: Monai valley: Free surface elevation at gauges 5 and 7.

14

5. Finite element solver for dispersive effects

Following the classical strategy [76], we now couple the non-dispersive hyperbolic solver to a second order solver for the physical weakly-dispersive effects. To this end, we propose to compute the auxiliary variable $\boldsymbol{\Psi}$ in (8) by means of a standard nodal P^1 (continuous) finite element (FE) method. Note that there is a notable change now in the meaning of the data associated to a mesh node i. The FV method evolves median dual cell averages which are in general different from the values of the variables at the nodes, used in the FE method. Similarly, we need to transfer from one representation to the other the derivatives of the depth and of the velocity appearing both in the coefficients in the operator T (equation (2) and equations (4)-(5)), and the right hand side where derivatives appear both in the definition of W and of R (cf. (10) and (3)). We will get back to this point in the next subsection.

The definitions of the operator T, $S_1(\cdot)$ and $S_2(\cdot)$, from (4) and (5) respectively, lead to the following variational form of the elliptic equation (8)

$$\int_\Omega v \cdot \boldsymbol{\Psi} + \alpha \int_\Omega S_1(v) \, h \, S_1\Big(\frac{\boldsymbol{\Psi}}{h}\Big) + \alpha \int_\Omega S_2(v) \, h \, S_2\Big(\frac{\boldsymbol{\Psi}}{h}\Big) = \text{RHS} + \text{BCs} , \tag{23}$$

or equivalently using (5)

$$\int_\Omega \left\{ \frac{1}{3}\Big(h\nabla \cdot v - \frac{3}{2}\nabla b \cdot v\Big)\Big(h^2\nabla \cdot \Big(\frac{\boldsymbol{\Psi}}{h}\Big) - \frac{3}{2}\nabla b \cdot \boldsymbol{\Psi}\Big) + \frac{1}{4}(\nabla b \cdot v)(\nabla b \cdot \boldsymbol{\Psi}) \right\} = \text{RHS} + \text{BCs} , \tag{24}$$

with RHS a variational approximation of the term $W - R$, and BCs the boundary condition terms which we briefly discuss below. The value of $\boldsymbol{\Phi}$, required in the hyperbolic step, is recovered nodally from (9).

To obtain a fully discrete approximation of (24) we now consider the finite element approximation

$$\boldsymbol{\Psi}_h = \sum_{K\in\Omega_h} \sum_{j\in K} \varphi_j \boldsymbol{\Psi}_j \tag{25}$$

where $\text{span}\{\varphi_j\}_{j\in\Omega_h}$ is the classical continuous P^1 finite element space. We similarly introduce discrete approximations h_h, b_h, η_h, and $\mathbf{u}_h$ for the elevations and velocity, as well as elemental discrete approximations of their first and second derivatives. Some options to provide these definitions and the solution we propose are discussed in the next subsection. The fully discrete variational form is expressed in terms of the array of the nodal values $\{\boldsymbol{\Psi}_j\}_{j\in\Omega_h}$, which by abuse of notation we also label $\boldsymbol{\Psi}$.

$$(\mathbb{M} + \alpha\mathbb{T}(h_h, b_h))\boldsymbol{\Psi} = \mathbb{W}(h_h, b_h) - \mathbb{R}(h_h, b_h, \mathbf{u}_h) \tag{26}$$

15

where the matrices on the left hand side are sparse 2×2 block matrices. In particular, $\mathbb{M}$ is the mass matrix with entries

$$[\mathbb{M}]_{ij}^{mn} = \delta_{mn} \sum_{K \in K_i \cap K_j} \int_K \varphi_i \, \varphi_j \, , \tag{27}$$

while the entries of $\mathbb{T}(h_h, b_h)$ are evaluated using the relation $h^2 \nabla \cdot (\boldsymbol{\Psi}/h) = h \nabla \cdot \boldsymbol{\Psi} - \boldsymbol{\Psi} \cdot \nabla h$ as

$$[\mathbb{T}(h_h, b_h)]_{ij}^{mn} = \sum_{K \in K_i \cap K_j} \int_K \left\{ \frac{1}{3} \left(h_h \partial_{X_m} \varphi_i - \frac{3}{2} \varphi_i \, (\partial_{X_m} b)_h \right) \left(h_h \partial_{X_n} \varphi_j - \frac{3}{2} \varphi_j \, (\partial_{X_n} b)_h - \varphi_j (\partial_{X_n} h)_h \right) \right.$$
$$\left. + \frac{1}{4} \varphi_i \, (\partial_{X_m} b)_h \, \varphi_j \, (\partial_{X_n} b)_h \right\} \tag{28}$$

Note that in the above expression the *mn* indices run over the spatial components of the unknown, while *ij* run over the mesh nodes.

Finally the right hand side terms are defined as

$$\mathbb{W}(h_h, b_h) = -\frac{g}{\alpha} \sum_{K \in K_i} \int_K \varphi_i \, h_h (\nabla \eta)_h \tag{29}$$

and

$$\mathbb{R}(h_h, b_h, \mathbf{u}_h) = \sum_{K \in K_i} \mathbb{R}^K$$

$$\mathbb{R}^K = -\frac{2}{3} \int_{\Omega_h} \nabla \varphi_i \, h_h^3 \left((\nabla u)_h \cdot (\nabla^\perp v)_h + (\nabla \cdot \mathbf{u})_h^2 \right) + \int_{\Omega_h} \varphi_i \, h_h^2 \left((\nabla u)_h \cdot (\nabla^\perp v)_h + (\nabla \cdot \mathbf{u})_h^2 \right) (\nabla b)_h$$

$$- \frac{1}{2} \int_{\Omega_h} \nabla \varphi_i \, h_h^2 \left((\mathbf{D}_b^{(2)})_h : (\mathbf{u}_h \otimes \mathbf{u}_h) \right) + \int_{\Omega_h} \varphi_i \, h_h \left((\mathbf{D}_b^{(2)})_h : (\mathbf{u}_h \otimes \mathbf{u}_h) \right) (\nabla b)_h \, . \tag{30}$$

having used the notation of section §4.1.1 for the Hessian of the bathymetry $\mathbf{D}_b^{(2)}$, and for its term by term product with the tesorized velocity.

Once the local polynomials representing h, b, $\mathbf{u}$ and their derivatives are defined over the element, all the above formulas can be evaluated by means of a sufficiently accurate quadrature formula. In practice we have used here a 6 points symmetric formula exact for polynomials of degree 4 taken from [25]. This definition is the objective of the next section.

6. Finite element/volume coupling: consistency and well-posedness considerations

This section provides some additional constraints on some of the numerical choices possible with the method proposed. These are justified by means of some theoretical (albeit heuristic) arguments, as well as

16

by strong numerical evidence. We consider first the issue of ensuring a compatible data representation in the two phases of the computation. This will give an indication on how to use FV data in the FE solver (and vice-versa). We then provide a few comments on the well-posedness of the overall procedure which show the importance of using dissipative numerical fluxes.

6.1. Consistency: using FV data in the FE solver and vice-versa

We start by recalling that the two approaches being used to solve the equations are based on different representation of the data. The FV scheme evolves the solution averages $\overline{\mathbf{U}}_i$ over the dual cells C_i, and local polynomials within the cells are reconstructed using essentially all the neighbouring information. The FE method uses a collocated nodal representation, and within each element the polynomial variation is obtained by interpolating the data available at the nodes.

Although both methods used unknowns associated to nodes, their meaning is substantially different. More importantly, the approximation of the derivatives has an impact on the accuracy of the right hand sides of the elliptic problem. For this reason we have chosen here to proceed as follows:

- when passing the FV solution to the elliptic solver we sample the reconstructed polynomials and their derivatives at the nodes:

$$f_i = \bar{f}|_{G_i} + \mathbf{D}_f^{(1)}|_{G_i} \cdot (\mathbf{x}_i - \mathbf{x}_{G_i}) + \frac{1}{2}\mathbf{D}_f^{(2)}|_{G_i} : \left(\delta_{G_i}^{(2)}(\mathbf{x}_i) - M_i^{(2)}\right).$$
$$(\nabla f)_i = \mathbf{D}_f^{(1,o2)}|_{G_i} + \mathbf{D}_f^{(2,o1)}|_{G_i} \cdot (\mathbf{x}_i - \mathbf{x}_{G_i}) \qquad (31)$$
$$(\mathbf{D}_f^{(2)})_i = \mathbf{D}_f^{(2,o1)}|_{G_i}$$

We then use these nodal values as a basis for a linear finite element approximation, so within any element $K \in \Omega_h$ we set:

$$f_h = \sum_{j \in K} \varphi_j f_j , \quad (\nabla f)_h = \sum_{j \in K} \varphi_j (\nabla f)_j , \quad (\mathbf{D}_f^{(2)})_h = \sum_{j \in K} \varphi_j (\mathbf{D}_f^{(2)})_j .$$

This, combined with the successive corrections method, allows to ensure on general meshes the second order of accuracy of all the first derivative terms (of h, b, and $\mathbf{u}$) appearing in (29), (30), and (28), and at least first order for the second derivatives of the bathymetry in (30). For configurations with high curvature in the topography, this is not enough and this value should be improved. A possible solution in relative simple cases, as those considered here, is to use the point-wise analytical value.

17

- The nodal finite element values $\boldsymbol{\Psi}_i$ are used to compote the post-processd average non-hydrostatic term

$$\overline{\boldsymbol{\Phi}}_i := \int\limits_{C_i} \boldsymbol{\Psi}_{\mathrm{h}} + \frac{g}{\alpha} \int\limits_{C_i} h_{\mathrm{h}}(\nabla\eta)_{\mathrm{h}}$$

this formula are evaluated by splitting the integral in local contributions over the quadrangular shapes $C_i \cap K$, then further splitting the quadrangles in triangles by joining the node i to the the gravity center of K, and then by using numerical quadrature on each sub-triangle.

Note that these choices have a direct impact on the theoretical accuracy attainable by the method. To see this, let us write an estimate on the local truncation error, for simplicity in the case of flat bathymetry.

We start by recasting (1) in dimensionless form. Using the standard fully nonlinear scaling leading to the Green-Naghdi system (see e.g.[45, 46] as well as [23] section §5) one easily shows that (6)-(9) can be written in dimensionless form as

$$\partial_t h + \nabla \cdot \mathbf{q} = 0$$
$$\partial_t \mathbf{q} + \nabla \cdot \left(\frac{\mathbf{q} \otimes \mathbf{q}}{h}\right) + h\nabla h = \mu(\boldsymbol{\Psi} + \frac{h}{\alpha}\nabla h) \qquad (32)$$
$$(I + \mu\,\alpha T)\boldsymbol{\Psi} = -\frac{h}{\alpha}\nabla h + hQ(\mathbf{u})$$

where we recall that $\mu = h_0^2/\lambda^2$ is the ratio of the reference depth on reference wavelength, and measures the shallowness and importance of dispersion. More importantly, as already recalled in the introduction, the above model is an approximation of the full non-linear free surface potential equations within an asymptotic error of $O(\mu^2)$ [45]. We now consider an exact smooth solution, and combine(32) with (11) to write the following local error:

$$TE_i = \frac{1}{|C_i|} \int\limits_{C_i} (\mathbf{U}_i^{\mathrm{ex}}(\mathbf{x}) - \mathbf{U}^{\mathrm{ex}}(\mathbf{x})) + \frac{1}{|C_i|} \int\limits_{C_i} \sum_{j \in D_i} \int\limits_{\partial C_{ij}} \left(\hat{\mathbf{F}}(\mathbf{U}_i^{\mathrm{ex}}(\mathbf{x}), \mathbf{U}_j^{\mathrm{ex}}(\mathbf{x})) - \mathbf{F}(\mathbf{U}^{\mathrm{ex}}(\mathbf{x}))\right)$$
$$+ \frac{\mu}{|C_i|} \int\limits_{C_i} \left(\Psi_h^{\mathrm{ex}} + \frac{h_{\mathrm{h}}^{\mathrm{ex}}}{\alpha}\nabla h_{\mathrm{h}}^{\mathrm{ex}} - \Psi^{\mathrm{ex}} - \frac{h^{\mathrm{ex}}}{\alpha}\nabla h^{\mathrm{ex}}\right) \qquad (33)$$

having denoted by $\mathbf{U}_i^{\mathrm{ex}}(\mathbf{x})$ the reconstructed polynomial obtained starting from the averages of a smooth exact solution $\mathbf{U}^{\mathrm{ex}}(\mathbf{x})$, and similarly by $h_{\mathrm{h}}^{\mathrm{ex}}$ the finite element approximation of exact nodal data. We can now proceed to a term by term estimation of the right hand side. The first one is by construction zero for quadratic polynomials, giving a rest of order $O(\mathrm{h}^3)$, and a similar result is easily proven for the second term (see e.g. [75] §2). The last one needs an estimate on the error of the solution of the elliptic step. Standard finite

18

element error estimates for elliptic equations (see e.g. [20, 27, 14]) rely firstly on a consistency estimates involving two main components: an estimate of the interpolation error for the solution, an estimate of the residual error, related to the approximation of the right hand side of the problem. For linear finite elements, the approximation error in L^2 norm is of an order $O(\mathrm{h}^2)$. Concerning the right and side, and inspection of (30) reveals that the limiting factor, for constant bathymetry, is the accuracy in the approximation of the derivatives of the velocity. This indicates that, *provided that the gradient approximation is second order accurate on general meshes the consistency of the scheme is of order $O(\mu\mathrm{h}^2)$, which is within the modelling error as soon as* $\mathrm{h} = O(\mu)$. The scheme is thus second order accurate wrt the mesh size. However when the shallow water sub-system is approximated to third order, we gain a factor μ in error without any increase in the cost of approximation of the elliptic problem which is the most computational intensive part of the model. Since μ is small in all applications for which the model is relevant, this gain is in principle non-negligible. This is essentially the same rationale behind the method of [76], extended to unstructured grids.

To confirm numerically the impact of these choices, we consider a travelling solitary wave which is an exact solution of the GN equations for $\alpha = 1$. Depth and velocity are known analytically and given by:

$$h(x, y, t) = h_0 + \alpha_0 \mathrm{sech}^2(k(x - c * t)) , \quad u(x, y, t) = c\left(1 - \frac{h_0}{h(x, y)}\right) \tag{34}$$

with h_0 the still water depth, α_0 the wave's amplitude, and with $k = \sqrt{3\alpha_0/4h_0^2(h_0 + \alpha_0)}$, and $c = \sqrt{g(h_0 + \alpha_0)}$. Although this is essentially a 1d solution, we have run it on 2D unstructured triangulations (rightmost picture on figure 4) to perform a grid convergence. We compare the results obtained by using the correctly sampled values of the solution and of its derivatives at the nodes, as discussed above (orange curve), against the result (blue curve) obtained by passing the nodal average as it is, and using it to construct the finite element approximation, including the elemental derivatives computed on each element as $(\nabla u)_\mathrm{h} = \sum_{j \in K} \nabla\varphi_j u_j$. The result shows the importance of accounting for the meaning of the data in the FE/FV coupling. Concerning the impact of using the extra correction in the polynomial reconstruction in the hyperbolic phase, we see that this relatively inexpensive extra iteration allows an error reduction roughly of a factor 5.

6.2. A comment on well-posedness

The choice of the numerical fluxes plays a fundamental for the robustness of the hyperbolic step in presence of irregular solutions for which the use of dissipative/upwind fluxes is necessary (cf. sections §4.1.3 and §4.2). When considering the propagation of smooth dispersive waves one may think that non-dissipative fluxes could be more appropriate. It turns out that for the method propose here this is not case,
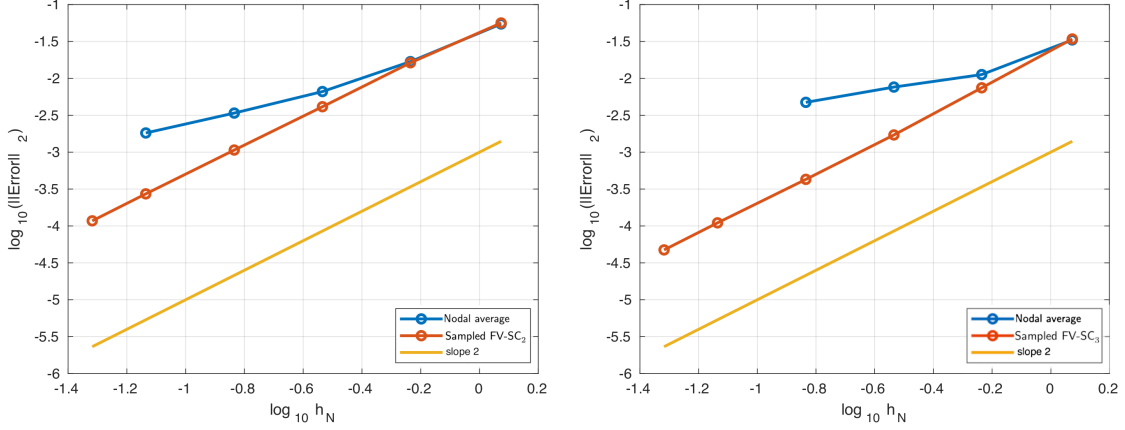
19

Figure 7: Error decay for the solitary wave. Left: hyperbolic step with second order successive correction. Right: hyperbolic step with third order successive correction. Orange: consistently sampled FV data used in the FE step. Blue: nodal averages in the FE step.

and numerical dissipation plays a major role also in the propagation region. To show this we will consider the simplified setting of the linearized dimensionless equations without bathymetry, which can be written as

$$(I - \alpha\mu(\nabla\nabla\cdot))\mathbf{\Psi} = -\frac{\nabla\eta}{\alpha}$$

$$\partial_t\eta + \nabla\cdot\mathbf{u} = 0 \tag{35}$$

$$\partial_t\mathbf{u} + \nabla\eta = \mu\mathbf{\Psi} + \mu\frac{\nabla\eta}{\alpha}$$

Despite the scheme having been derived and coded for the above form, for the discussion of this section it is more appropriate to start from the more classical formulation

$$\partial_t\eta = -\nabla\cdot\mathbf{u}$$

$$(I - \alpha\mu(\nabla\nabla\cdot))\partial_t\mathbf{u} = -(I - (1-\alpha)\mu(\nabla\nabla\cdot))\nabla\eta \tag{36}$$

The operator to be inverted to evolve the velocity $\mathbf{u}$ (as well as to pre-compute $\mathbf{\Psi}$) is a grad-div operator quite common in the modelling of e.g. electromagnetic waves. The important aspect of this type of equation is that if is naturally formulated in the functional space of vectors $H(\mathrm{div})$, as its variational form involves the scalar product

$$(\mathbf{v}, \mathbf{u})_\Omega := \int_\Omega \mathbf{v}\cdot\mathbf{u} + \alpha\mu\int_\Omega \nabla\cdot\mathbf{v}\cdot\nabla\cdot\mathbf{u} \tag{37}$$

which readily generates the equivalent squared $H(\mathrm{div})$ norm $\mathbf{u}^2 + \alpha\mu(\nabla\cdot\mathbf{u})^2$. It is well known that, despite the symmetry of the bilinear form induced by the equation, H^1 finite elements as the one used here to solve the

20

elliptic problem are not well posed as prone to spurious modes related to the rotational of the solution. For electromagnetic waves this is a long time known fact [21, 22, 34]. Divergence conforming elements allow of course to side-step this issue.

To use H^1 elements, which are easier to implement, and better suited to be coupled with a hyperbolic solver something needs to be done. Usually, this is achieved by introducing, at the PDE level or in the scheme, a regularizing operator that stabilizes the spurious modes otherwise not controlled by the incomplete norm generated by the variational formulation (or equivalently (37)). In our method this is essentially the case. However, we do not modify the elliptic solver. The stabilization is embedded in the hyperbolic evolution step, and associated to the form of the upwind finite volume numerical fluxes which embed a discrete Laplacian which plays a crucial role.

To provide some heuristics into this mechanism, we consider the following regularized explicit discrete in time linear equivalent of the GN system

$$
\begin{aligned}
\frac{\eta^{n+1} - \eta^n}{\Delta t} - \nabla \cdot (\epsilon_{\mathrm{h}}^{\eta} \nabla \eta)^n &= -\nabla \cdot \mathbf{u}^n \\
(I - \alpha\mu(\nabla\nabla\cdot))\frac{\mathbf{u}^{n+1} - \mathbf{u}^n}{\Delta t} - \nabla \cdot (\epsilon_{\mathrm{h}}^{\mathbf{u}} \nabla \mathbf{u})^n &= -(I - (1-\alpha)\mu(\nabla\nabla\cdot))\nabla\eta^n
\end{aligned}
\tag{38}
$$

The regularization here is explicitly added in the form of artificial diffusion terms, which in reality stems from the use of upwind numerical fluxes. The above system can be seen as some space continuous equivalent of the fully discrete scheme, somewhat similarly to the modified equation in finite difference methods [?]. In particular, the coefficients $\epsilon_{\mathrm{h}}^{\eta}$ and $\epsilon_{\mathrm{h}}^{\mathbf{u}}$ depend on the numerical flux. For the dimensionless linearized problem under consideration, these can be both approximated by $\epsilon_{\mathrm{h}}^{\eta} = \epsilon_{\mathrm{h}}^{\mathbf{u}} \approx \mathbb{C}\,\mathrm{h}$ for some mesh dependent constant $\mathbb{C}$ which we assume for simplicity to be diagonal. Note that this implies that the divergence acting in the second term in each equation is applied line by line.

To show the impact of numerical dissipation we proceed as follows. We start by introducing at each time step the Helmholtz/Hodge decomposition of the velocity vector [38, 39, 9]

$$
\mathbf{u}^n = \nabla\phi_1^n + \nabla^{\perp}\phi_2^n
\tag{39}
$$

where the orthogonal nabla operator $\nabla^{\perp} = (\partial_y, -\partial_x)$ being the equivalent of the rotational in the 2D plane. We then introduce this decomposition into the second in (38), and look for closure equations for the two potentials. Using the div-free property of the second component of the decomposition, the first relation we

can write is that

$$\frac{\nabla^\perp \phi_2^{n+1} - \nabla^\perp \phi_2^n}{\Delta t} + (I - \alpha\mu(\nabla\nabla\cdot))\frac{\nabla\phi_1^{n+1} - \nabla\phi_1^n}{\Delta t} - \nabla \cdot (\epsilon^{\mathbf{u}}\nabla\mathbf{u})^n = -(I - (1-\alpha)\mu(\nabla\nabla\cdot))\nabla\eta^n \quad (40)$$

We now apply the $-\nabla^\perp\cdot$ operator, and use the identity $\nabla^\perp \cdot \nabla = 0$. This allows to write

$$-\nabla^\perp \cdot \frac{\nabla^\perp \phi_2^{n+1} - \nabla^\perp \phi_2^n}{\Delta t} + \nabla^\perp\nabla \cdot (\epsilon_{\mathrm{h}}^{\mathbf{u}}\nabla\mathbf{u})^n = 0 \quad (41)$$

The first conclusion we can draw is that for $\epsilon_{\mathrm{h}}^{\mathbf{u}} = 0$ then an admissible solution is that ϕ_2 is constant in time. In other words, at any time step *the velocity field is defined up to an and arbitrary rotational component* $\nabla^\perp\phi_2$ *not seen by the scheme. This is essentially a spurious mode, which is not controlled and may prevent the discrete solution to converge*.

We now consider the case in which the numerical dissipation is present. With the hypothesis that $\epsilon_{\mathrm{h}}^{\mathbf{u}}$ is diagonal and that the $\nabla\cdot$ is applied line by line, simple manipulations show that

$$-\nabla^\perp \cdot \nabla^\perp \phi_2 = -\Delta\phi_2$$
$$\nabla^\perp\nabla \cdot (\epsilon_{\mathrm{h}}^{\mathbf{u}}\nabla\mathbf{u})^n = -\Delta^2\phi_2 \quad (42)$$

with Δ the usual Laplace operator. This allows to write (40) as

$$-\Delta\left(\frac{\phi_2^{n+1} - \phi_2^n}{\Delta t} - \epsilon_{\mathrm{h}}^{\mathbf{u}}\Delta\phi_2^n\right) = 0 \quad (43)$$

For uniform and homogeneous boundary conditions, we may deduce that

$$\frac{\phi_2^{n+1} - \phi_2^n}{\Delta t} - \epsilon_{\mathrm{h}}^{\mathbf{u}}\Delta\phi_2^n = 0 \,. \quad (44)$$

This shows that *in presence of numerical dissipation spurious rotational effects are smoothed according to a parabolic operator with a smoothing rate proportional to the numerical dissipation.*

We propose some numerical evidence to confirm the above observations by studying again the grid convergence of the solitary wave solution (34). We perform the following experiment. On one hand we solve the nonlinear shallow water equations forced with $\mathbf{\Phi} = \mathbf{\Phi}^{\mathrm{exact}}$ obtained by replacing (34) in the momentum equation. This corresponds to imposing the solitary wave as a manufactured solution (cf [65]). On the other we solve the full system including the dispersive terms for which (34) is an exact solution if $\alpha = 1$. In both cases, we perform a grid convergence with centered numerical fluxes, as well as with the full upwind flux.

22

We perform the computations up to time $t = 0.1$ on 7 unstructured meshes starting with a triangulation with 328 triangles, and then halving the mesh size. The results are reported in figure 8 for the second order (left), and third order (right) polynomial reconstruction in the hyperbolic fluxes. For the shallow water equations all configurations converge. The centered fluxes fail to provide third order of accuracy, at least on the meshes considered, however full second order is observed. For the GN system, the error obtained with centered fluxes quickly stalls, and error or even solution blow-up is observed on the last meshes for the final time considered. Full convergence is restored with the upwind fluxes, confirming our heuristics that numerical dissipation is sufficient to control the growth of spurious modes.
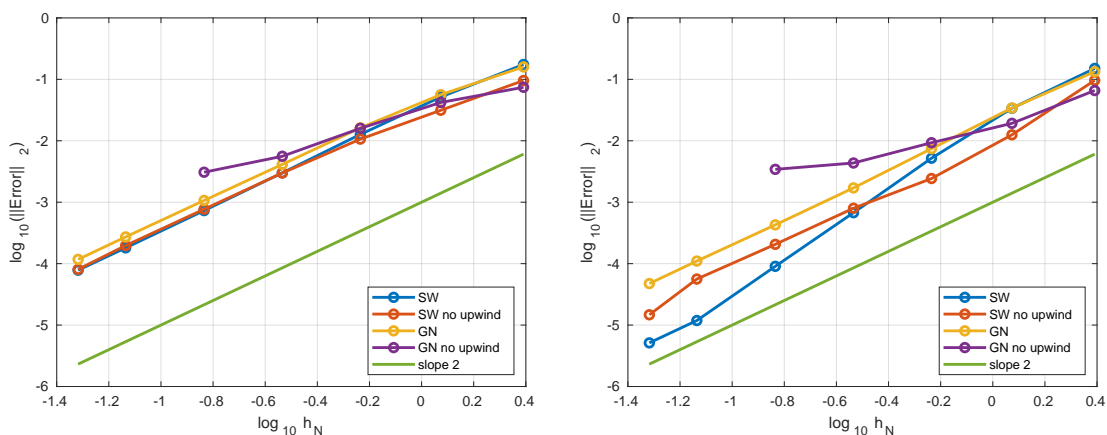
Figure 8: Solitary wave. Left: second order successive correction. Right: third order successive correction. Blue: shallow water with upwind fluxes and manufactured solution. Orange: shallow water with centered fluxes and manufactured solution. Yellow: Green-Naghdi with upwind fluxes. Magenta: Green-Naghdi with ventered fluxes.

7. Time continuous spectral analysis: dispersion error and stability

To further characterize the scheme proposed, we briefly discuss the results of a time continuous spectral analysis in the 1D case. We recall that the exact enhanced Green-Naghdi equations have a phase defined by:

$$\omega_{gn}^2 = gh_0 k^2 \frac{1 + \frac{\alpha-1}{3}k^2 h_0^2}{1 + \frac{\alpha}{3}k^2 h_0^2}, \tag{45}$$

having denoted by k the wavenumber. To characterise the dispersion error, we need to replace a Fourier mode into our scheme. So we assume that for a wavenumber k, the solution has the form $\mathbf{U} = \mathbf{U}_0 e^{v_h t + jkx}$,

with j the imaginary unit, and where $\nu_h = \xi_h + j\omega_h$ and ξ_h, ω_h represent the discrete amplification rate and phase. As done to couple the FV and FE method, one has to be careful here not to confuse cell averages with nodal values. We can indeed find that

$$\bar{\mathbf{U}}_i = \int_{x_{i-1/2}}^{x_{i+1/2}} \mathbf{U}_0 e^{\nu t + jkx} = \frac{\mathbf{U}_i}{j\mu_h}(e^{j\frac{\mu_h}{2}} - e^{-j\frac{\mu_h}{2}}) = \frac{\mathbf{U}_i}{j\mu_h} 2\sin(\frac{\mu_h}{2}) \qquad (46)$$

with $\mathbf{U}_i = \mathbf{U}_0 e^{\nu_h t + jkx_i}$, and $\mu_h = kh$. Using this relation consistently, and replacing in the one-dimensional version of the scheme we obtain

$$j(\nu_h C - B)\eta_i + h_0 A u_i = 0$$
$$gA\eta_i + j(\nu_h C - B)u_i = -\mu_h \frac{1}{h_0} M^{FV} D\eta_i. \qquad (47)$$

The right hand side of the second equation is the inverse of the Fourier symbol of the finite element discretization of the elliptic equation reducing in 1D to a Poisson equation (cf. e.g. [31]). The coefficients A, B, C D are reported in Appendix B for completeness. The impact of the definition of the matrix M^{FV} arising depending on the quadrature of $\mathbf{\Phi}$ is also provided. Only the best results are left here for clarity. These are obtained when all matrices are evaluated exactly. Straightforward computations show that

$$\omega_h^2 = (ghA^2 + \mu M^{FV} AD)/C^2. \qquad (48)$$

Figure 9 plots the relative dispersion errors (rde) $|\omega_s - \omega_{gn}|/\omega_{gn}$ with respect to the dispersion relation of the eGN equations (45). For comparison, we also plot the dispersion errors of sake of reference we are also plotting the relative dispersion errors that comes when using 1. a second and fourth order finite difference schemes (see [31, 64] for the full expressions). The pictures show that dispersion error of the scheme presented in this paper is smaller or close to the one of FD4 depending the number of nodes per wavelength. For completeness we also plot on figure 10 the error $|\omega_s - \omega_{\text{airy}}|/\omega_{\text{airy}}$ with respect to the exact dispersion relation $\omega_{\text{airy}}^2 = gk^2 \tanh(kh_0)$). We observe a compensation between discretization error and modelling error so that the scheme has a lower error w.r.t the exact dispersion relation than it has wrt the Green-Naghdi one. This is related to the interaction of the phase advance/lag error of the scheme and the form of the phase of the Boussinesq model. This could be in the future a design criterion for low order (second and third) schemes.

7.1. Stability and dissipation

While the well-posedness in 2D can be justified with the arguments of section §6.2, in one dimension the Fourier analysis provides a characterization of the linear stability of monochromatic waves in terms of
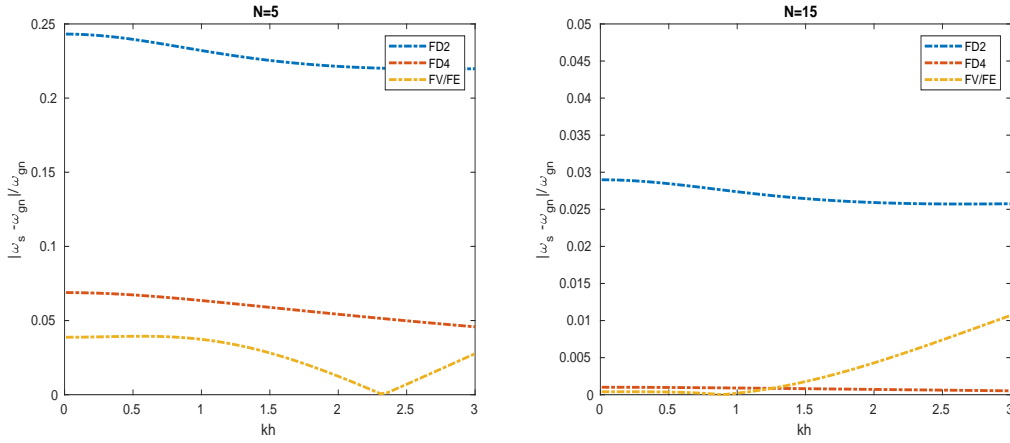
24

Figure 9: Dispersion error with respect to ω_{gn} for nodes per wave length $N = 5$ and $N = 15$
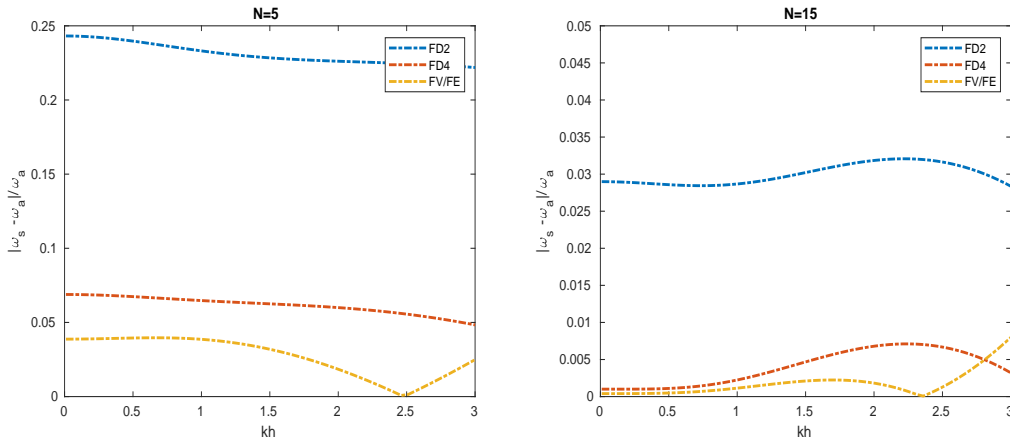

Figure 10: Dispersion error with respect to ω_{airy} for nodes per wave length $N = 5$ and $N = 15$

the discrete wave amplification rate ξ_h. In particular, for the upwind schemes we can obtain from system (47) the relation

$$\xi_h = \frac{B}{C} \tag{49}$$

where the coefficients B and C are reported in Appendix B for the case of third and second order successive recontructions. Figure 11 plots the numerical wave amplification for three different choices of number of points per wavelength. We can see that the amplification rate is negative, which means the schemes

25
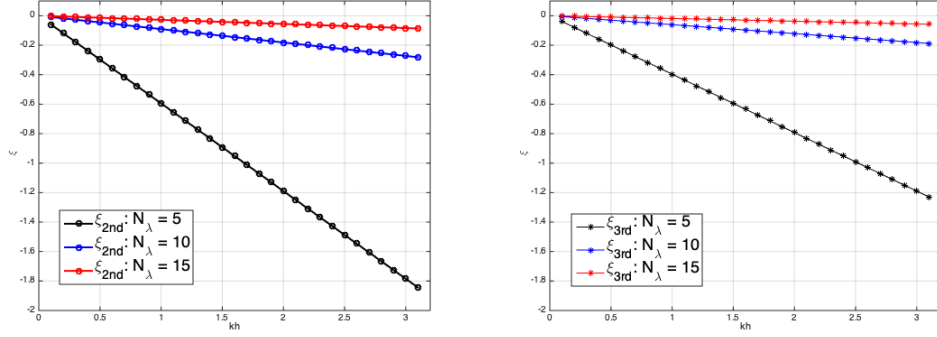
Figure 11: Numerical amplification rate as a function of the reduced wavenumer kh when using the second (left) and the third (right) order reconstruction in the hyperbolic part, for different choices of the number of points per wavelength N_λ

are stable. Of course the presence of damping constrains somewhat the number of nodes per wavelength required to resolve long time/distance propagation, although considerably less for the third order scheme, as the plot suggests. For the fully centered discretizations, the spectral analysis provides systematically $\xi_h = 0$.

8. Boundary conditions, wave generation, and wave breaking closure

8.1. Wave breaking detection and closure

A hybrid strategy for wave breaking treatment is implemented in the scheme. We first estimate the location of breaking waves using explicit criteria, then we apply the NLSW equations to solve the flow in breaking regions and the GN ones elsewhere. Following the work of [42], we use the combination of the two above phase-resolving criteria for the triggering mechanism:

- the surface variation criterion: $|\eta_t| \geq \gamma \sqrt{gh}$ with $\gamma \in [0.35, 0.65]$

- the local slope angle criterion: $\|\nabla \eta\| \geq \tan \phi_c$ with ϕ_c the critical angle value.

The values of γ and ϕ_c are depending on the type of the breaker. The first criterion flags for breaking when η_t is positive, since breaking starts on the front face of the wave, while the second criterion, acting complementary to the first, is useful for the detection of hydraulic jumps. In this work the value of $\phi_c = 30^o$ is used. Moreover, the estimation of the Froude number of the wave is used to established when to switch of

the breaking and to detect non-breaking bores. A practical implementation of the breaking mechanism can be found in [42, 31, 29].

8.2. *Wave generation and boundary conditions*

In this work, we have implemented periodic, fully reflective/wall and absorbing boundary conditions. For the walls for all boundary nodes we modify the elliptic solver to set the conditions

$$\mathbf{\Phi} \cdot \mathbf{n} = 0 \Rightarrow \mathbf{\Psi} \cdot \mathbf{n} = -h \frac{\nabla \eta \cdot \mathbf{n}}{\alpha}$$

$$\partial_{\mathbf{n}} \mathbf{\Phi} \cdot \tau = 0 \Rightarrow \partial_{\mathbf{n}} (\mathbf{\Psi} \cdot \tau + h \frac{\nabla \eta \cdot \tau}{\alpha}) = 0$$

For straight walls the first condition is a consequence of $\mathbf{u} \cdot \mathbf{n} = 0$, while the second forces the rotational components of $\mathbf{\Phi}$ to zero at the walls, which is consistent with the condition $\nabla \wedge \mathbf{\Phi} = 0$ which can be easily proved for the continuous equation used in the bulk. In practice we modify both the RHS and matrix of the elliptic system to account for these conditions. In the hyperbolic solver we also make sure that $\mathbf{u} \cdot \mathbf{n} = 0$ by modifying the hyperbolic fluxes and source and removing the normal component.

Absorbing boundaries are also applied in order to dissipate completely the energy of the incoming waves, trying at the same time to eliminate any non-physical reflection. This kind of boundaries requires the definition of a sponge layer in which the surface elevation and the momentum are damped by multiplying their values by the coefficient:

$$m(\mathbf{x}) = \sqrt{1 - \left(\frac{\mathbf{x} - d(\mathbf{x})}{L_s} \right)^2}.$$

where L_s is the sponge layer width and $d(\mathbf{x})$ is the normal distance between the cell center with coordinates $\mathbf{x}$ and the absorbing boundary. Typical values of the sponge width are related to the wave length λ of the incoming wave and usually are: $\lambda \leq L_s \leq 1.5\lambda$.

A large number of numerical tests demand the generation of monochromatic waves. One very common approach is to use an internal wave generator. This means, generating the waves in the computational domain avoiding complications that boundaries can create. In this work we, thus, make use of an internal wave generator, first described in [77]. It is obtained by adding a source term to the mass equation. More details on the topic can be found in [64].

9. Numerical validation and benchmarking

9.1. Grid convergence for the solitary wave

We return to the exact solitary wave to compare on figure 12 the errors obtained when using the second (blue lines) and third order (orange lines) reconstructions. Convergence plots are reported for the free surface, and for Φ. We observe that using the third order scheme in the hyperbolic step, thus passing from $O(\text{h}^2)$ to $O(\mu \text{h}^2)$, allows a more or less consistent reduction of the error by a factor between 3 and 5.
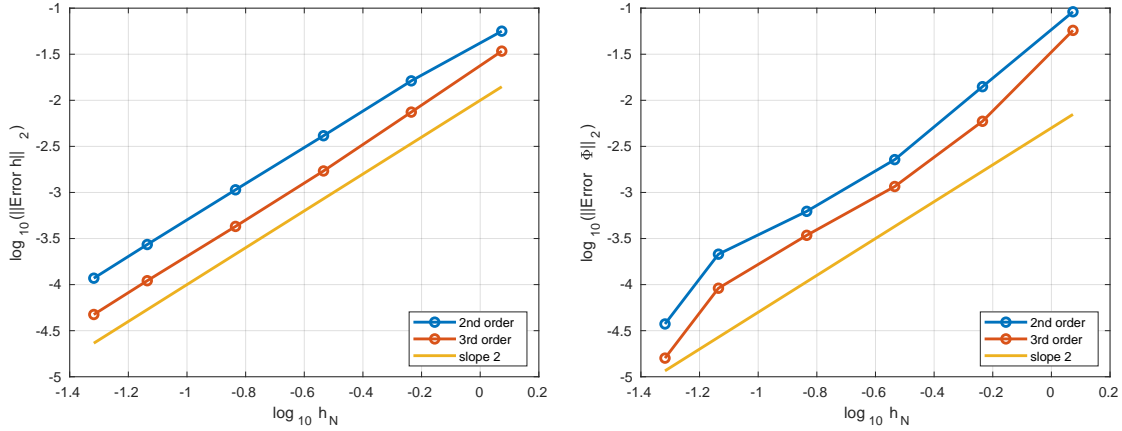
Figure 12: Error decay for second and third order schemes for h and Φ .

9.2. Circular shoal

Whalin [78] studied the focusing effected induced by a semi-circular shoal on wave trains of different periods. The wave tank used is of $6.096m$ wide and $25.6m$ long. A semi-circular shoal was placed at the middle portion of the tank leading the water depth to decrease from $0.4572m$ at the wave maker region to $0.1524m$ to the end of the tank. This test case has been used by many authors in order to test the dispersive properties of their models, see for example [50, 6, 72, 28, 70, 41, 64] were a detailed description of the set up of the case can be found. The three test cases that have been reproduced here are:

(a) $T = 1s, A = 0.039m, h_0/\lambda=0.306$ and $\epsilon = 0.085$

(b) $T = 2s, A = 0.015m, h_0/\lambda=0.117$ and $\epsilon = 0.033$

(c) $T = 3s, A = 0.0136m, h_0/\lambda=0.075$ and $\epsilon = 0.030$

where T is the wave period, A the wave height and λ the wave length. Wave gauges are placed along the center line to record the time series of the free surface elevation, which are analysed in the frequency domain using a Discrete Fourier Transform (DFT) to obtain the first three harmonic amplitudes. The computational domain used is $[-10, \ 36] \times [0, \ 6.096]m$. Periodic waves are generated using the internal generator placed at $x = 4m$ and sponge layers of $6m$ are placed at the left and right end of the domain. Reflective boundary conditions are imposed at the remaining boundaries. For the computation of the first case a triangular grid was used, consisting of triangles with side lengths $h_x = 0.05m$ and $h_y = 0.1m$ leading to a mesh of $N = 56211$ nodes. For the last two cases the grid consists of equilateral triangles, with $h_N = 0.01m$ leading to a mesh of $N = 28151$ nodes. The CFL value used was 0.5.

For all the test cases the incoming waves are linear in the deeper portion of the tank and they are steepening due to the wave shoaling. Wave energy gradually spreads out to higher harmonics, which increase in amplitude in the shoaling region. For both case (a) and (b) the agreement between the numerical and experimental data is quite satisfactory for all the harmonics while in the last test case (c) the numerical results overestimates the first harmonic and underestimates the other two. This behavior has also been observed by other authors [50, 6, 70, 48] and the discrepancies are attributed to the shorter evolution distance of this test case or to the presence of free reflected waves. We compare the numerical solution obtained using the third order scheme (continuous line) and the second order scheme (dashed line) in the hyperbolic part. The difference, as expected, is more pronounced in the first two cases were the waves are shorter.

9.3. Elliptic shoal

This test case studies the refraction and diffraction of a regular wave over a complex bathymetry and it is a reproduction of the experiment of [7]. It is mainly used to verify models based on mild-slope equations but also the extended Boussinesq-type equations. The numerical domain is 20m wide and 22m long, with $x \in [-10, \ 10]$ and $y \in [-17, \ 15]$. The bathymetry consists of an elliptic shoal placed on a ramp of constant slope forming a 20° angle with the x axis. The maximum water depth is $h_0 = 0.45m$ at the wave maker's position which is placed at $y = -13m$. The bathymetry set up can be found in [41, 64] and references therein. The monochromatic wave's characteristics are: period $T = 1s$ and amplitude $a = 0.0232m$ corresponding to a non linearity degree $\epsilon = a/h = 0.3$. The normalized time average wave height was measured in eight different sections (see figure). Wall boundary conditions are imposed on the left and right boundaries, while sponge layers of $4m$ are placed and the bottom and top ends of the domain. In this test case an unstructured grid was used, which is refined in the region of the shoal. In particular the grid size in the y direction varies
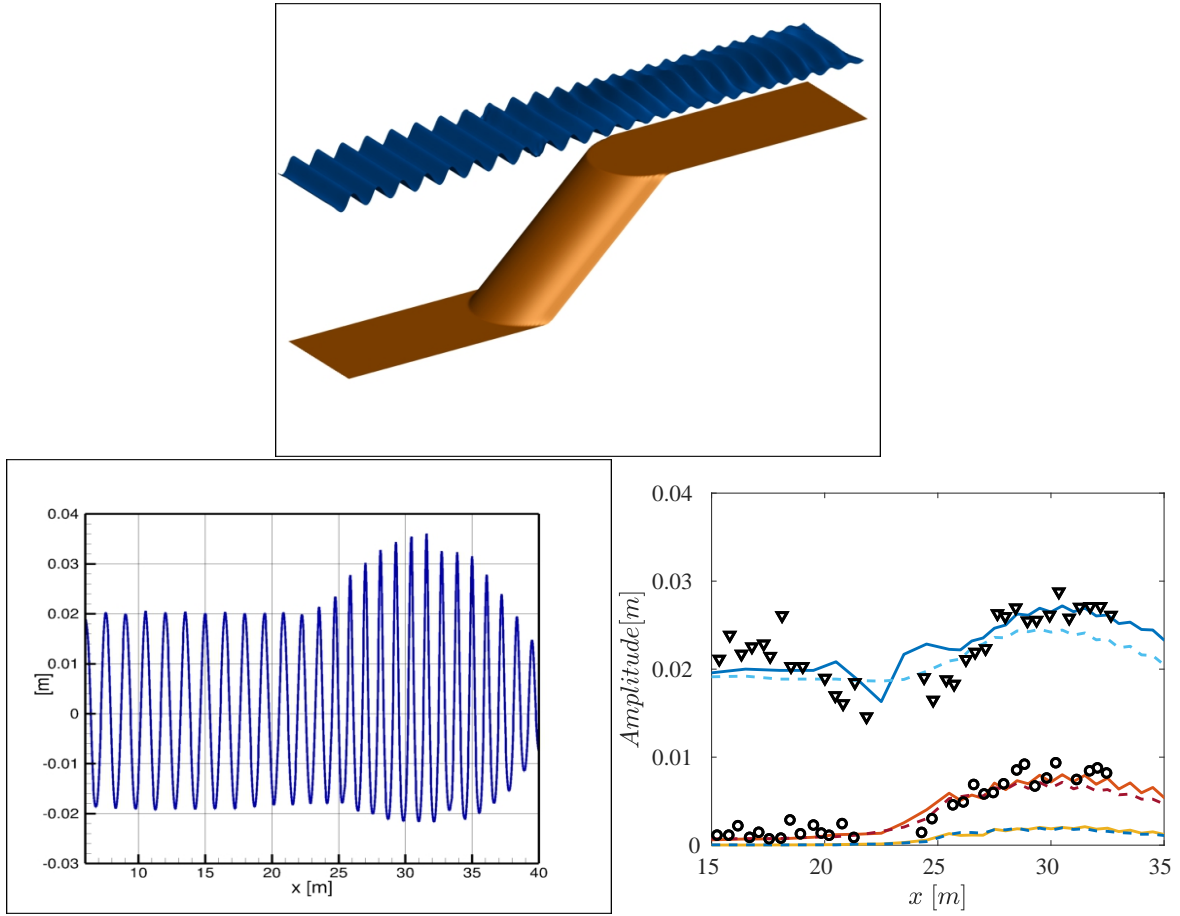
29

Figure 13: Wave diffraction over a semi-circular shoal. Case (a): Left: Computed free surface data along the centerline of the domain. Right: comparison of the DFT of the numerical data over the centerline with experimental data. Dashed line second order scheme, continuous line third order scheme.

from $h_y \approx 0.1m$ on the top and bottom boundaries to $h_y = 0.05m$ in the region around the shoal. The simulation period is 50s. and the *CLF* used is 0.5. A three dimensional view of the water elevation at the final time is reported on figure 16. In order to compare the numerical results with the experimental data [7], time dependent data have been extracted, the last $25sec$ of the simulation, from the sections 1-8. The time series of the surface elevation are analysed using the zero-up crossing technique to isolate single waves and to compute the averaged wave height. The results are normalised by the incoming wave height $2a = 0.0464m$ and are reported on figures 17 and 18. The agreement on the numerical results and the experimental data are satisfactory and comparable to the results given by the literature ([64],[70], [72]).
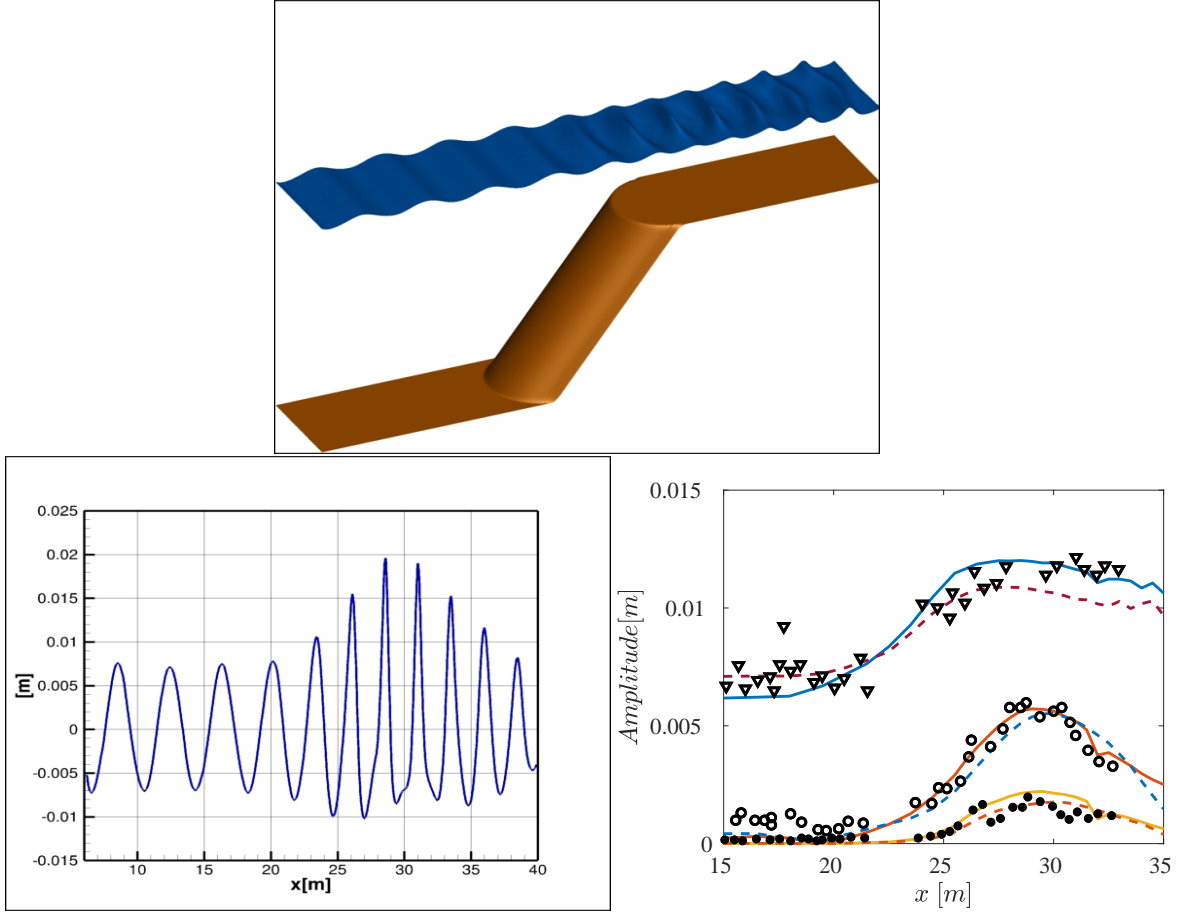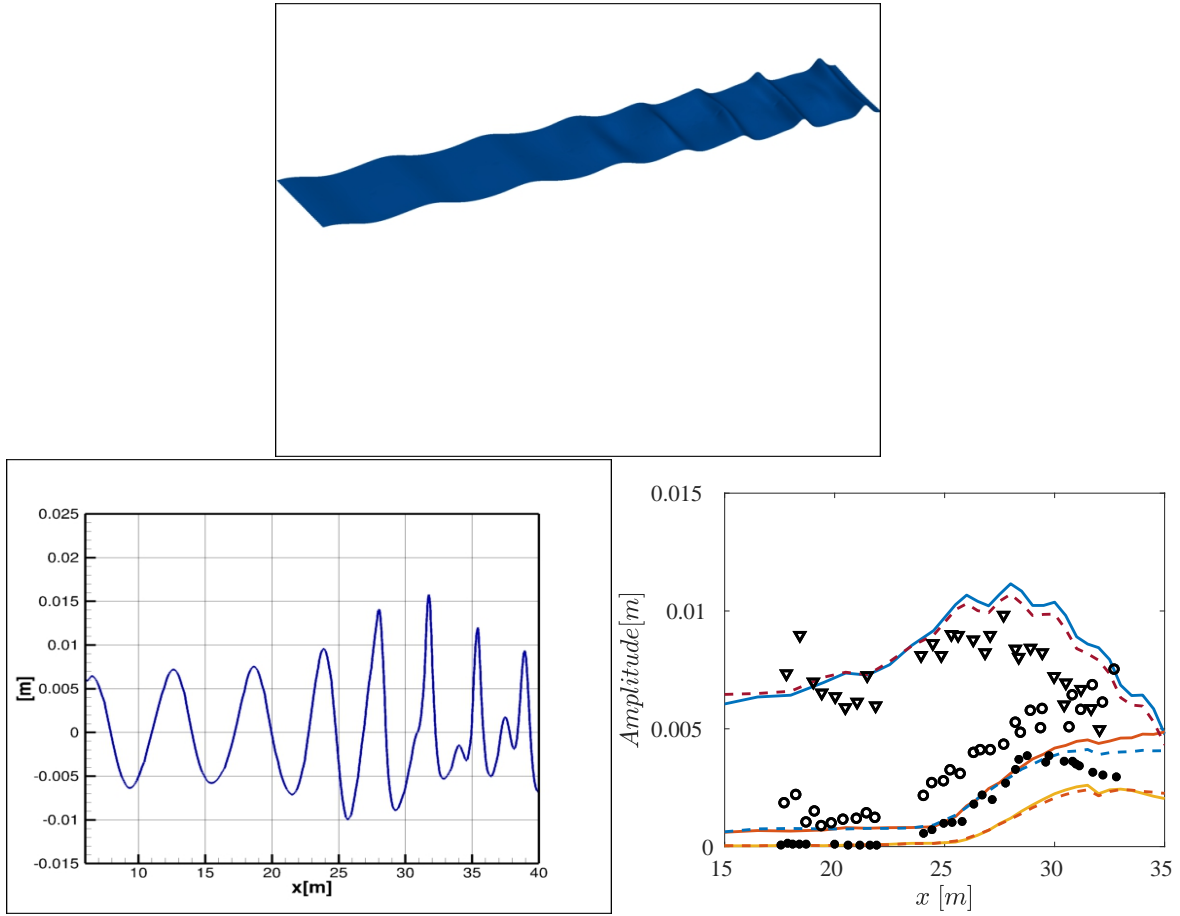
Figure 14: Wave diffraction over a semi-circular shoal. Case (b): Left: Computed free surface elevation at time $t = 40$sec. Right: comparison of the DFT of numerical data over the center-line with experimental data. Dashed line second order scheme, continuous line third order scheme.

9.4. Solitary interacting with a cylinder

In this test case we examine numerically the propagation and scattering of a solitary wave with a vertical cylinder. The laboratory experiment [24] investigates the interaction of the wave with the cylinder and it has been used by [40, 41] and references therein to validate their numerical models. The numerical domain used here is $x \times y \in [0, \ 14m] \times [0, \ 0.55m]$. A vertical cylinder of diameter $0.16m$ was placed at $(x_0, y_0) = (8.5, 0.275)$. The solitary has amplitude $A = 0.0375m$ and placed at $x = 4m$. The undisturbed water depth is $h_0 = 0.15m$ so the nonlinearity of the wave is $\epsilon = 0.25$. Six wave gauges were recording the free surface elevation located at: $wg1 = (8.4, \ 0.275), wg2 = (8.5, \ 0.170), wg3 = (8.5, \ 0.045), wg4 =$

31

Figure 15: Wave diffraction over a semi-circular shoal. Case (b): Left: Computed free surface elevation at time t = 40sec. Right: comparison of the DFT of the numerical data over the center-line with experimental data. Dashed line second order scheme, continuous line third order scheme.

$(8.6,\ 0.275), wg5\ =\ (8.975,\ 0.275), wg6\ =\ (9.375,\ 0.275)$. The mesh has 11345 nodes and is refined around the cylinder. Figure 19 presents the 3d view of the free surface elevation after 4 sec, when the solitary interacts with the cylinder. This interaction causes the generation of scattering waves that propagate downstream while the rest of the wave recovers to a solitary wave and propagates upstream. The first wave that interacts with the cylinder and propagates upstream is computed quite accurately compared to the experimental data as seen in figures 20-22. The reflected waves, even though are better resolved compared to the ones that can be found in the bibliography [40, 41] , presents some discrepancy compered to the experimental data. This may indicates that a fully dispersive model is needed for this case.

32
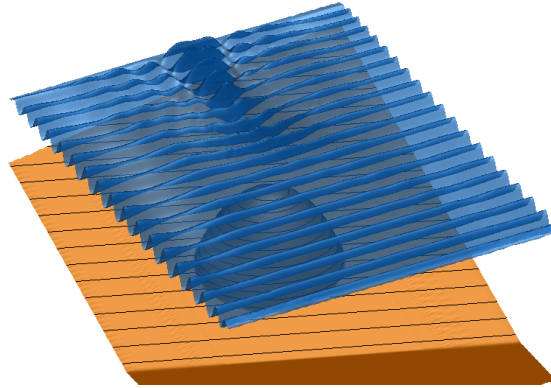
Figure 16: Wave diffraction over an elliptic shoal: 3D view of the free surface elevation at time $t = 50sec$.

9.5. Solitary wave breaking on a 3D reef

Swigler et Lynett (2011) performed laboratory experiments at the O.H. Hinsdale Wave Research Laboratory of Oregon State University to study the specific phenomena which occurs when a tsunami like wave approaches the coast, such as shoaling, refraction, breaking and run-up. Many authors have used this case to validate their codes, since it is quite demanding and involves multiple physical phenomena. The computational domain is 48.8m long and 26.5m wide. Figure 23 shows the test set up along with the position of the wave gauges. The topography is determined from a laser scan and it consists of a slope of 1:30 connected with a triangular reef flat submerged between 0.75m and 0.9m below the still water level. The offshore shelf edge has an elevation of 0.71m with the apex located at x=12.6m. The steepest slope of the shelf is at the apex and becomes milder moving along the shelf edge toward the basin side walls. A concrete cone is also placed at the apex of the reef between x=14m and 20m. It has a diameter of 6m and a height of 0.45m The planar beach continues up to x=31m and then becomes level until the back of the basin. Nine wave gauges were placed into the basin in order to measure the variation of the free surface elevation: gauges 1, 2, 3, 7 were located at $y = 0m$ and $x = 7.5, 13, 21, 25m$ gauges 4, 5, 6, 8 were located at $y = 5m$ and $x = 7.5, 13, 21, 25m$, while gauge 10 have been set at $y = 10m$ and $x = 25m$.

Compared to the experimental case, the computational domain has been extended from $x = 0m$ to $x = 5m$ in order to be able to completely contain the initial solitary wave. It has been discretized by means of two
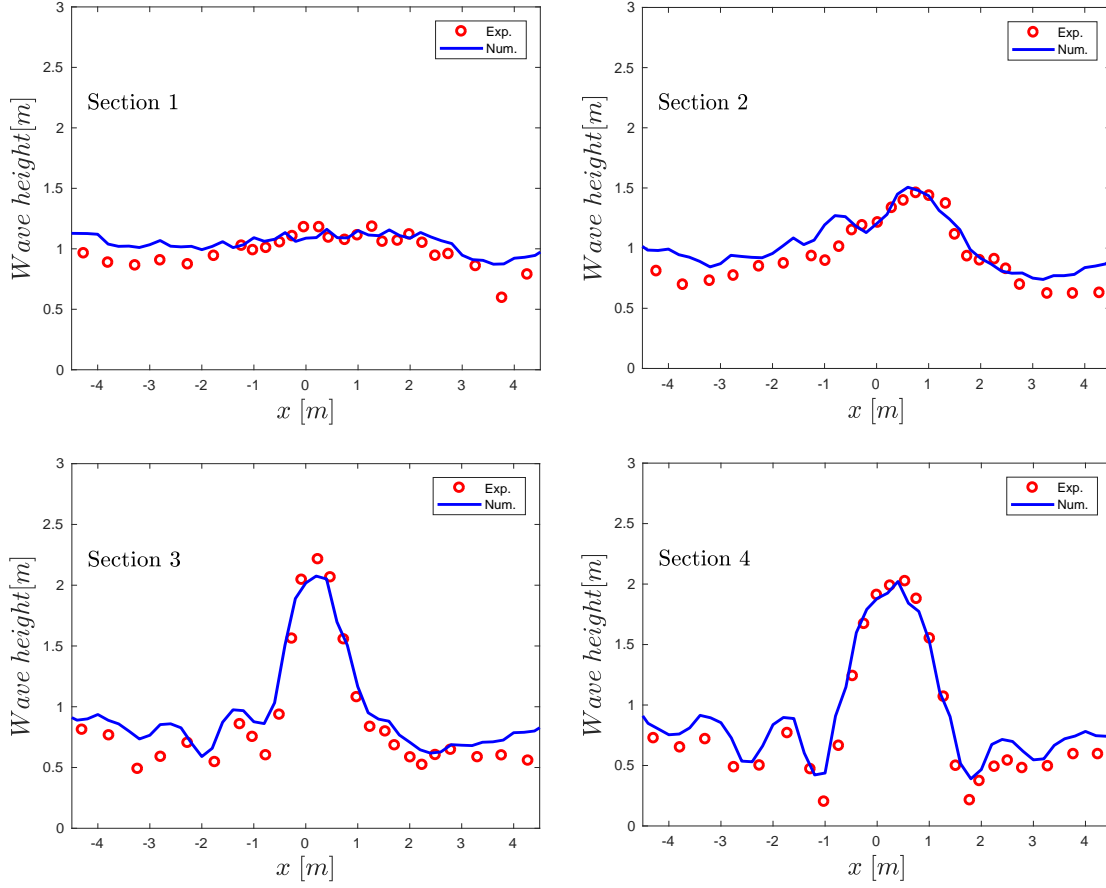
33

Figure 17: Wave diffraction over an elliptic shoal: Normalised wave height from sections 1 to 4.

non-uniform unstructured grids. The first one is adapted to the bed curvature, as shown in 23, and characterized by reference maximum and minimum size respectively: $\max(h_K) = 0.3m$ and $\min(h_K) = 0.125m$. The second one is a triangular, non-refined grid of $h_k = 0.3$ A solitary wave of amplitude $A = 0.39m$, corresponding to $\epsilon = 0.5$, is initially placed in $x = 0$ and wall reflecting boundary conditions are imposed in each boundary of the domain. We used a Manning coefficient $N_m = 0.014$ for representing bed roughness. A CFL number of 0.5 was used, together with $\gamma = 0.6$ for the breaking detection criterion.

Figure 24 shows the computed free water surface at different time instants, using the refined mesh. With white color we denote the time evolution of the breaking regions detected by the criteria of the breaking mechanism. As the solitary wave propagates towards the beach it shoal, increases its steepness and nonlin-
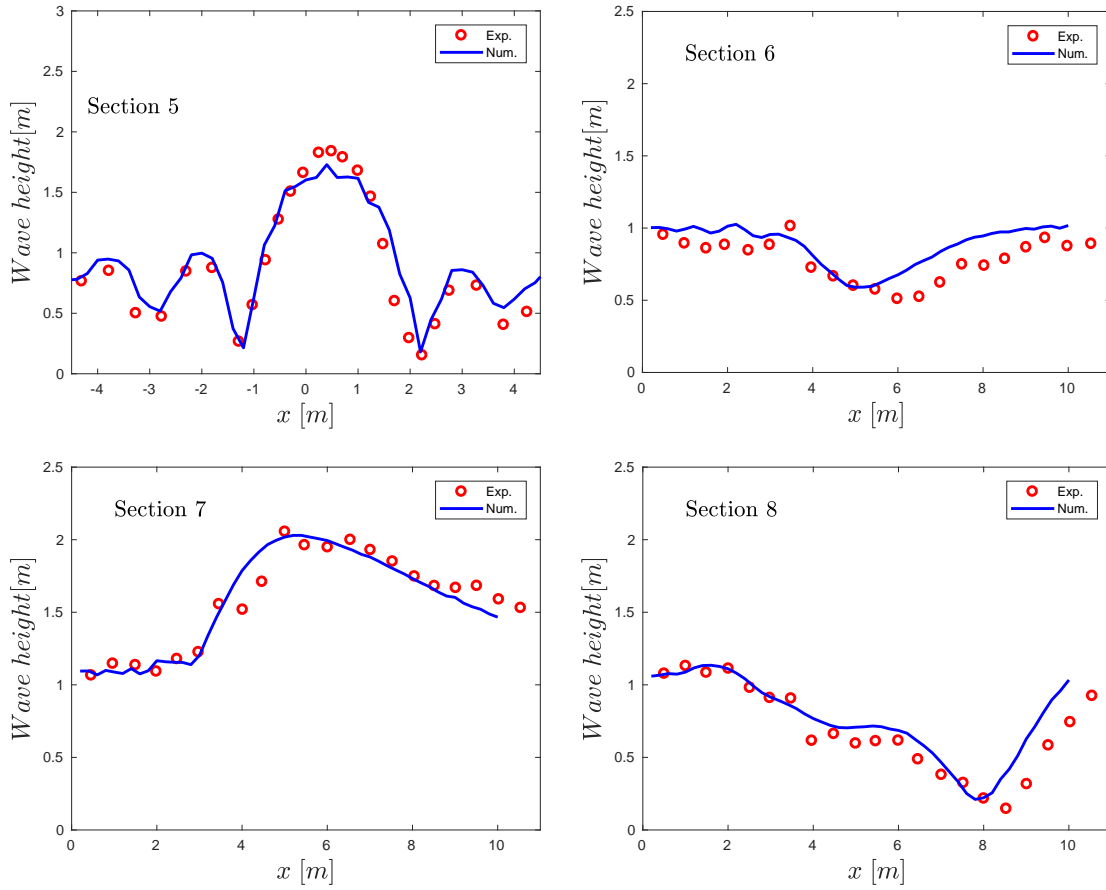
Figure 18: Wave diffraction over an elliptic shoal: Normalised wave height from sections 5 to 8.

earity, up to reaching a breaking point at $t = 5$ on the center line of the domain, when it reaches the apex of the triangular shelf. At $t = 6.5s$ the central part of the wave has completely overtopped the concrete cone, while on the two sides, the surge continues to shoal, diffracting around the base of the cone. By $t = 8.5s$, the refracted and diffracted waves collide on the lee side of the shelf. After $t = 9s$, the water starts to withdraw from the con top and a bore-front forms, from the combined waves after the diffraction, and propagates on the shelf behind the cone and then onshore. After $t = 15s$, a new bore is creates from the the drawn-down of the water and collides with the refracted waves.

The next figure 25 plots the computed free surface time series on the wave gauges 1- 9 against the experimental data using the two grids. Green color represents the numerical results obtained using the

35
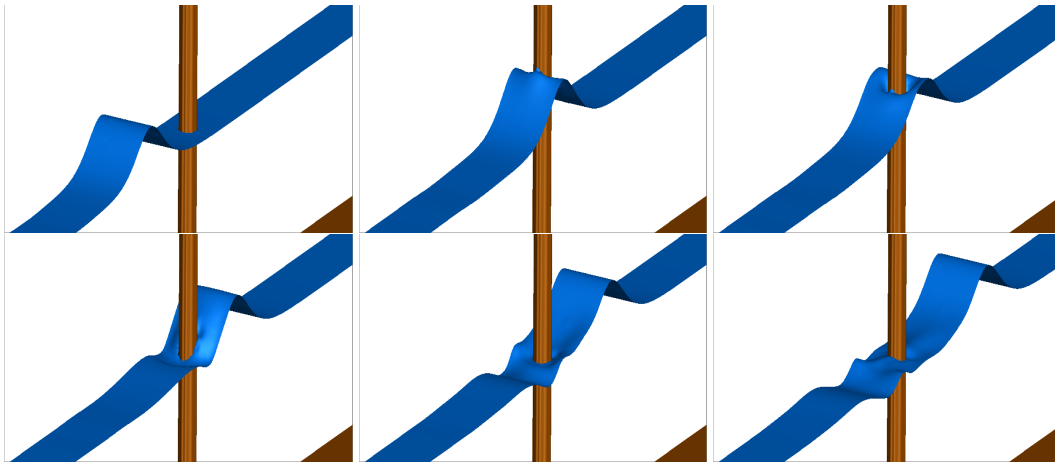
Figure 19: 3D view of the free surface elevation. Interaction of the solitary wave with the vertical cylinder.
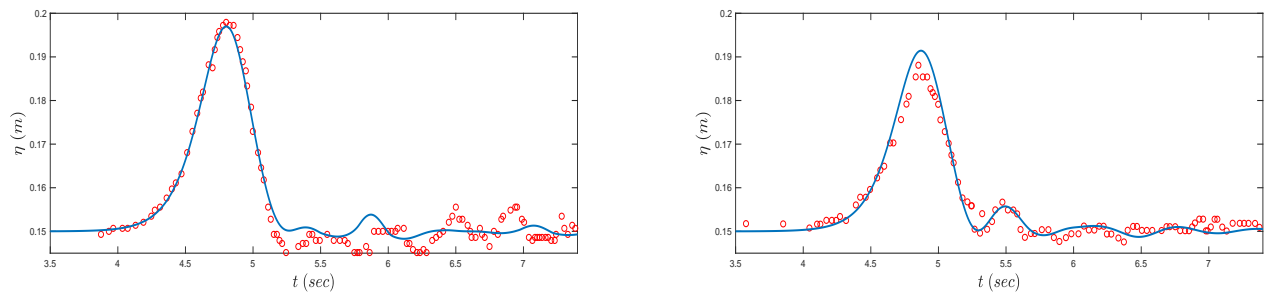
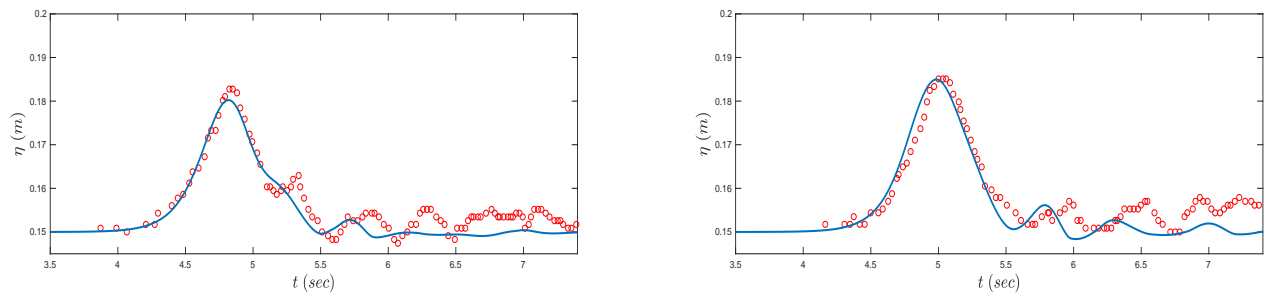Figure 20: Free surface elevation at wave gauges 1 and 2

Figure 21: Free surface elevation at wave gauges 3 and 4

coarser mesh and blue color the ones obtained using the refined mesh. Both cases show the same behavior, although the results obtained with the coarser mesh are more diffusive in the secondary waves, as expected.
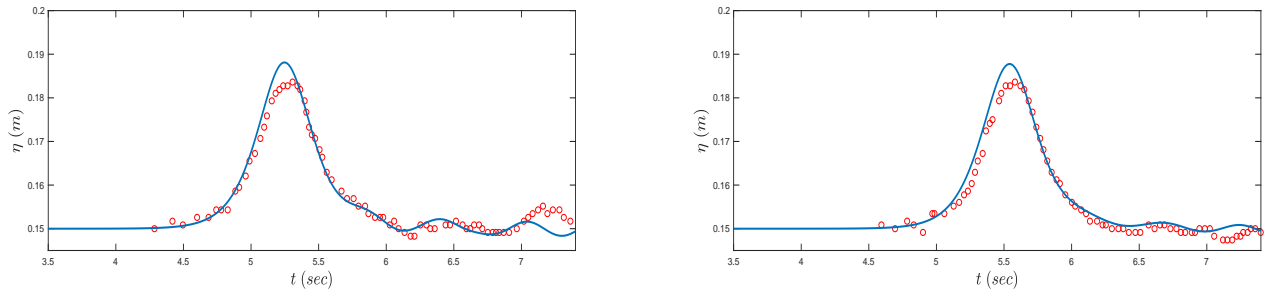
36

Figure 22: Free surface elevation at wave gauges 5 and 6
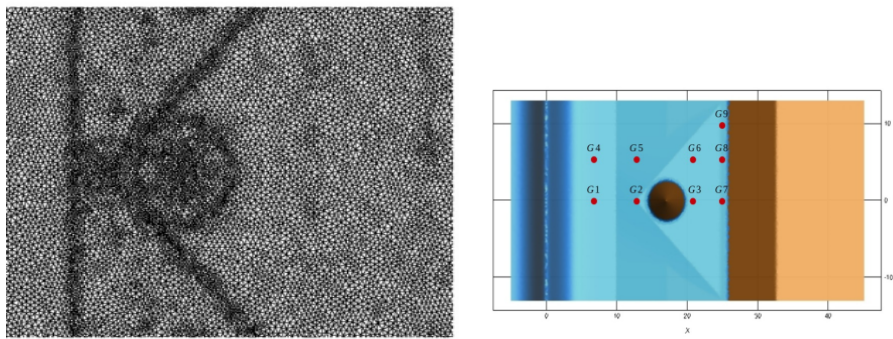
Figure 23: Solitary wave propagation over a three dimensional reef: Close up view of the adapted mesh used for the computation(right) and positioning of wave gauges (left)

The arrival of the first incoming wave is correctly captured in gauges 1 and 2, as it is for the refracted and diffracted waves at the lee side of the cone, as can be seen from gauge 3. The signal at the gauges located at the north side of the cone indicates that wave shoaling, breaking and propagation on the shelf is accurately predicted, together with the complex nonlinear interaction between diffracted and refracted waves.

9.6. The seaside experiment

This final test case examines the impact of a tsunami on an urban area. The laboratory benchmark took place in the Oregon State University and has been served as a blind benchmark test case for the NTHMP Mapping and Modeling Benchmarking Workshop: Tsunami Currents (`http://coastal.usc.edu/currents_workshop/index.html`). A physical and numerical comparison presented in [58]. It has also been used in the project TANDEM (`http://www-tandem.cea.fr`) as a benchmark test case. It involves a complex topography including a seawall and several buildings inspired of the real city of Oregon

37

at 1:50 scale. It is a very demanding test case since it tests the ability of the model to simulate flows in complex and real topography. It involves wave propagation , shoaling wave breaking and flooding in an urban area involving wet/dry fronts. The rectangular basin was 48.8m long 26.5m wide, 2.1m deep and was equipped with a piston type wave maker with a maximum stroke of 2.1m and maximum velocity of 2 m/sec. Details in the physical experiment can be found in [58]. The data available involves a detailed topography, the forcing signal the positions as well as the time histories of water height and velocity in a large number of wave gauges in the streets of the city model. The numerical wave tank is $x \times y \in$ and an unstructured triangular mesh of $N = 172854$ is used with a min $h_{ref} = 0.03$. The mesh is refined in the region where the buildings are placed. The individual structures and buildings are approximated as steep-sided topography and a manning coefficient of 0.01 is used. The CFL number is set to 0.3 and the the breaking parameters are $\gamma = 0.3$ and $tan(\phi_c) = 0.37$.

The incoming wave enters from the left boundary and wall boundary conditions are imposed in the remaining boundaries. In the domain, 31 wave gauges measure the free surface elevation and the velocity . Figure 26 sows the measurement locations in the onshore region. Furthermore, four surface wave gauges were fixed in the basin at the following locations: $wg1 = (2.086, -0.515), wg2 = (2.068 \ 4.065m), wg3 = (18.618, \ 0.000m)$ and $wg4 = (18.618, \ 2.860m)$. Time series comparison of the free surface elevation between the experimental data and the numerical ones at Locations A, B, C, D are shown in figures 28, 29, 30, 31 respectively. In all figures we perform comparison for the GN equations (blue line) and the NSWE (black line). Figure 32 presents the comparison of the free surface elevation between the experimental and numerical data in the wave gauges WG1-WG4.

10. Conclusions

In this work we presented a hybrid numerical approach for the solution of the Green-Naghdi equations on unstructured meshes. We split the original system in a hyperbolic and an elliptic part. For the hyperbolic part, we used a a third order in space, node centered FV scheme. We achieve a third order reconstruction of the physical variables by means of a successive correction method which iteratively improves derivatives computed by means of the standard Green-Gauss formula. This approach guarantees third order accuracy even on unstructured meshes. In order to prevent oscillations on non smooth solutions we used a slope limiter [54] applied for a first time on a node centered scheme using the derivative reconstruction via the successive correction. We coupled the non-dispersive hyperbolic solver to a second order solver for the physical weakly dispersive effects. We used the standard P1 FE method. We ensured compatible data representation in the

38

two phases of the computations since both methods evolve unknowns associated to the nodes, but with a totally different meaning.

We examined the impact of those data representation on the theoretical accuracy by writing an estimate of the local truncation error for constant bathymetry concluding that providing a second order accurate gradient on general meshes the consistency of the scheme is of order $O(\mu h^2)$. The importance of accounting for the meaning of the data in the FE/FV coupling has also been confirmed by performing a convergence test.

An other conclusion of this work is related to the choice of the numerical fluxes in the hyperbolic step. It turns out that we have to use dissipative/upwind fluxes in order to stabilize the incomplete norm generated by the variational formulation, since we use H^1 finite elements, in the elliptic step. We provided numerical evidences to confirm this fact by studying again grid convergence.

Finally we showed that when using the third order scheme in the hyperbolic step, allows a consistent reduction of the error by a factor between 3 and 5.

Acknowledgments

Appendix A.

For a C_i a computational cell the geometric tensor of order k is given by

$$\frac{1}{C_i} \int \int_{C_i} (\mathbf{x} - \mathbf{x_{G_i}})^{\otimes k} \, dS$$

with $\otimes$ the tensor product. This means for a third order scheme ($k = 2$) we will have to define before the beginning of our computations the geometric moments:

$$
\begin{aligned}
(XY)_i &= \frac{1}{|C_i|} \int_{C_i} (x - x_{G_i})(y - y_{G_i}) dS, \\
(X^2)_i &= \frac{1}{|C_i|} \int_{C_i} (x - x_{G_i})^2 dS, \\
(Y^2)_i &= \frac{1}{|C_i|} \int_{C_i} (y - y_{G_i})^2 dS.
\end{aligned}
$$

The construction of the M_2 matrix is based on the calculation of three specific mesh depended variables

$$\alpha_i = \frac{x_{G_i}^2 + (X^2)_i}{2},$$

$$\beta_i = \frac{y_{G_i}^2 + (Y^2)_i}{2},$$

$$\gamma_i = x_{G_i} y_{G_i} + (XY)_i$$

where G is the cell's center of gravity and X_i^2, Y_i^2, XY_i are the second order momentum of the cell C_i. Then, M_2^{-1} is a 3×3 matrix and is computed using the second derivatives of the moments. It is defined as:

$$M_2 = \begin{bmatrix} (\alpha_i)_{xx} & (\beta_i)_{xx} & (\gamma_i)_{xx} \\ (\alpha_i)_{yy} & (\beta_i)_{yy} & (\gamma_i)_{yy} \\ ((\alpha_i)_{xy} + (\alpha_i)_{yx})/2 & ((\beta_i)_{xy} + (\beta_i)_{yx})/2 & ((\gamma_i)_{xy} + (\gamma_i)_{yx})/2 \end{bmatrix}$$

Appendix B.

We report here the coefficients of system (47) presented in section 7 and involved in the dispersion properties of the scheme. From the discretization of the hyperbolic part using the FV scheme with the third order reconstruction we easily obtain system (47) with :

$$A = \frac{k}{\mu} \left(\frac{81}{48} \cos(\frac{3\mu}{2}) - \frac{69}{48} \cos(\frac{\mu}{2}) - \frac{13}{48} \cos(\frac{5\mu}{2}) + \frac{1}{48} \cos(\frac{7\mu}{2}) \right) \tag{B.1}$$

$$B = \frac{ck}{\mu} \left(-\frac{115}{48} \sin(\frac{\mu}{2}) + \frac{61}{48} \sin(\frac{3\mu}{2}) - \frac{15}{48} \sin(\frac{5\mu}{2}) + \frac{1}{48} \sin(\frac{7\mu}{2}) \right) \tag{B.2}$$

$$C = 2\sin(\frac{\mu}{2}). \tag{B.3}$$

When we use the second order reconstruction then the coefficients are:

$$A = \frac{k}{\mu} \left(-\frac{6}{4} \cos(\frac{\mu}{2}) + \frac{7}{4} \cos(\frac{3\mu}{2}) - \frac{1}{4} \cos(\frac{5\mu}{2}) \right) \tag{B.4}$$

$$B = \frac{ck}{\mu} \left(-\frac{10}{4} \sin(\frac{\mu}{2}) + \frac{5}{4} \sin(\frac{3\mu}{2}) - \frac{1}{4} \sin(\frac{5\mu}{2}) \right) \tag{B.5}$$

and C is the same as before.

From the solution of the elliptic problem we get:

$$D = \frac{-gh^3}{3} T^G \left(M^G \right)^{-1} \left(M^G - \frac{ah^2}{3} S^G \right)^{-1} \quad \text{and} \tag{B.6}$$

$$M^{FV} = \frac{1}{8} (6 + 2\cos(\mu)) \tag{B.7}$$

where

40

- The galerkin mass matrix: $M^G = \frac{1}{6}(4 + 2\cos(\mu))$

- second order space derivatives: $S^G = \frac{k^2}{\mu^2}(2\cos(\mu) - 2)$

- third order space derivatives: $T^G = \frac{k^3}{2\mu^3}(2\sin(2\mu) - 4\sin(\mu))$.

In a similar way to [31], we analyse in figure B.33 different discretization possibilities with or without mass lumping on M^{FV} and M^G matrices in figure B.33. Now the curves are obtained for two values $kh = 0.5$ and $kh = 2.5$, corresponding to a long and to a shorter wave (or shallow and deep waters respectively) and plotted against the inverse number of the number of nodes per wavelength. The optimum choice that minimizes the rde is not to lump any matrix, which was also the case for the 1DH scheme of [31]. This choice is thus employed in this work.

References

[1] MB Abbott, HM Petersen, and O Skovgaard. Computations of short waves in shallow water. In Coastal Engineering 1978, pages 414–433. 1978.

[2] TIMOTHY BARTH. Recent developments in high order k-exact reconstruction on unstructured meshes. In 31st Aerospace Sciences Meeting, page 668, 1993.

[3] Timothy Barth and Paul Frederickson. Higher order solution of the euler equations on unstructured grids using quadratic reconstruction. In 28th aerospace sciences meeting, page 13, 1990.

[4] Timothy J Barth. Aspects of unstructured grids and finite-volume solvers for the euler and navier-stokes equations. 1992.

[5] T.J. Barth. Aspects of unstructured grids and finite-volume solvers for the euler and navier-stokes equations. 1992. AGARD, Special Course on Unstructured Grid Methods for Advection Dominated Flows.

[6] S Beji and K Nadaoka. A formal derivation and numerical modelling of the improved boussinesq equations for varying depth. Ocean Engineering, 23(8):691–704, 1996.

[7] JCW Berkhoff, N Booy, and A C₋ Radder. Verification of numerical wave propagation models for simple harmonic linear water waves. Coastal Engineering, 6(3):255–279, 1982.

[8] A. Bermudez, A. Dervieux, J.-A.e Desideri, and M.E. Vazquez. Upwind schemes for the two-dimensional shallow water equations with variable depth using unstructured meshes. Computer Methods in Applied Mechanics and Engineering, 155(1):49–72, 1998.

[9] Harsh Bhatia, Gregory Norgard, Valerio Pascucci, and Peer-Timo Bremer. The helmholtz-hodge decomposition—a survey. IEEE Transactions on Visualization and Computer Graphics, 19(8):1386–1404, 2013.

[10] Philippe Bonneton, Eric Barthélemy, Florent Chazel, Rodrigo Cienfuegos, David Lannes, Fabien Marche, and Marion Tissier. Recent advances in serre–green naghdi modelling for wave transformation, breaking and runup processes. European Journal of Mechanics-B/Fluids, 30(6):589–597, 2011.

[11] Philippe Bonneton, Florent Chazel, David Lannes, Fabien Marche, and Marion Tissier. A splitting approach for the fully nonlinear and weakly dispersive green–naghdi model. Journal of Computational Physics, 230(4):1479–1498, 2011.

[12] Joseph Boussinesq. Théorie des ondes et des remous qui se propagent le long d'un canal rectangulaire horizontal, en communiquant au liquide contenu dans ce canal des vitesses sensiblement pareilles de la surface au fond. Journal de mathématiques pures et appliquées, pages 55–108, 1872.

[13] Pierre Brenner. Unsteady flows about bodies in relative motion. In 1st AFOSR Conference on Dynamic Motion CFD Proceedings, Rutgers University, New Jersey, USA, 1996.

[14] S. Brenner and R. Scott. The Mathematical Theory of Finite Element Methods, volume 15 of Texts in Applied Mathematics. Springer, 2008.

[15] P. Brufau, P. Garcia-Navarro, and M. E. Vazquez-Cendon. Zero mass error using unsteady wetting–drying conditions in shallow flows over dry irregular topography. International Journal for Numerical Methods in Fluids, 45(10):1047–1082, 2004.

[16] M.J. Castro, J.M. Gonzalez-Vida, and C. Pares. Numerical treatment of wet/dry fronts in shallow water flows with a modified roe scheme. Mathematical Models and Methods in Applied Sciences, 16(6):897–931, 2006.

[17] Aurore Cauquis, Mario Ricchiuto, and Philippe Heinrich. Lax–wendroff schemes with polynomial extrapolation and simplified lax–wendroff schemes for dispersive waves: A comparative study. Water Waves, pages 1–33, 2022.

[18] Florent Chazel, David Lannes, and Fabien Marche. Numerical simulation of strongly nonlinear and dispersive waves using a green–naghdi model. Journal of Scientific Computing, 48(1-3):105–116, 2011.

[19] Vincent P Chiravalle and Nathaniel R Morgan. A 3d lagrangian cell-centered hydrodynamic method with higher-order reconstructions for gas and solid dynamics. Computers & Mathematics with Applications, 78(2):298–317, 2019.

[20] P.G. Ciarlet. The finite element method for elliptic problems, volume 4 of Studies in Mathematics and its Applications. North-Holland Publishing Co., 1978.

[21] M. Costabel. A coercive bilinear form for maxwell's equations. Journal of Mathematical Analysis and Applications, 157(2):527–541, 1991.

[22] M. Costabel and M. Dauge. Weighted regularization of maxwell equations in polyhedral domains. a rehabilitation of nodal finite elements. Numerische Mathematik, 93:239–277, 2002.

[23] M.W. Dingemans. Water wave propagation over uneven bottoms. Advanced Series on Ocean Engineering. 1997.

[24] JS Antunes Do Carmo, FJ Seabra Santos, and E Barthélemy. Surface waves propagation in shallow water: a finite element model. International Journal for Numerical Methods in Fluids, 16(6):447–459, 1993.

[25] D.A. Dunavant. High degree efficient symmetrical gaussian quadrature rules for the triangle. Int. J. Numer. Methods in Engrg., 21:1129–1148, 1985.

[26] Arnaud Duran and Fabien Marche. A discontinuous galerkin method for a new class of green–naghdi equations on simplicial unstructured meshes. Applied Mathematical Modelling, 45:840–864, 2017.

[27] A. Ern and J.-L. Guermond. Theory and practice of finite elements, volume 159 of Applied Mathematical Sciences. Springer, 2004.

[28] Claes Eskilsson, SJ Sherwin, and Lars Bergdahl. An unstructured spectral/hp element model for enhanced boussinesq-type equations. Coastal Engineering, 53(11):947–963, 2006.

[29] Andrea Gilberto Filippini. Free surface flow simulation in estuarine and coastal environments: numerical development and application on unstructured meshes. PhD thesis, Bordeaux, 2016.

[30] Andrea Gilberto Filippini, Stevan Bellec, Mathieu Colin, and Mario Ricchiuto. On the nonlinear behaviour of boussinesq type models: Amplitude-velocity vs amplitude-flux forms. Coastal Engineering, 99:109–123, 2015.

[31] Andrea Gilberto Filippini, Maria Kazolea, and Mario Ricchiuto. A flexible genuinely nonlinear approach for nonlinear wave propagation, breaking and run-up. Journal of Computational Physics, 310:381–417, 2016.

[32] Albert E Green and Paul M Naghdi. A derivation of equations for wave propagation in water of variable depth. Journal of Fluid Mechanics, 78(2):237–246, 1976.

[33] ST Grilli, R Subramanya, IA Svendsen, and J Veeramony. Shoaling of solitary waves on plane beaches. Oceanographic Literature Review, 8(42):608, 1995.

[34] L. Hagg and M. Berggren. On the well-posedness of galbrun's equation. Journal de Mathématiques Pures et Appliquées, 150:112–133, 2021.

[35] Florian Haider. Discrétisation en maillage non structuré général et applications LES. PhD thesis, 2009.

[36] Florian Haider, Pierre Brenner, Bernard Courbet, and Jean-Pierre Croisille. Efficient implementation of high order reconstruction in finite volume methods. In Finite Volumes for Complex Applications VI Problems & Perspectives, pages 553–560. Springer, 2011.

[37] Florian Haider, Bernard Courbet, and Jean-Pierre Croisille. A high-order compact reconstruction for finite volume methods: the one-dimensional case. 2015.

[38] H. Helmholtz. Uber integrale der hydrodynamischen gleichungen, welche den wirbelbewegungen entsprechen. J.fur die reine und angewandte Mathematik, 1858(55):25–55, 1858.

[39] H. Helmholtz. On integrals of the hydrodynamical equations, which express vortex-motion. Philosophical Magazine and J. Science, 33(226):485–512, 1867.

[40] Theodoros Katsaounis, Dimitrios Mitsotakis, and George Sadaka. Boussinesq-peregrine water wave models and their numerical approximation. Journal of Computational Physics, page 109579, 2020.

[41] M Kazolea, AI Delis, IK Nikolos, and CE Synolakis. An unstructured finite volume numerical scheme for extended 2d boussinesq-type equations. Coastal Engineering, 69:42–66, 2012.

44

[42] M Kazolea, Argiris I Delis, and Costas E Synolakis. Numerical treatment of wave breaking on unstructured finite volume approximations for extended boussinesq-type equations. Journal of Computational Physics, 271:281–305, 2014.

[43] Maria Kazolea and AI Delis. Irregular wave propagation with a 2dh boussinesq-type model and an unstructured finite volume scheme. European Journal of Mechanics-B/Fluids, 72:432–448, 2018.

[44] David Lannes. The water waves problem: mathematical analysis and asymptotics, volume 188. American Mathematical Soc., 2013.

[45] David Lannes and Philippe Bonneton. Derivation of asymptotic two-dimensional time-dependent equations for surface water wave propagation. Physics of fluids, 21(1):016601, 2009.

[46] David Lannes and Fabien Marche. A new class of fully nonlinear and weakly dispersive green–naghdi models for efficient 2d simulations. Journal of Computational Physics, 282:238–268, 2015.

[47] Maojun Li, Liwei Xu, and Yongping Cheng. A cdg-fe method for the two-dimensional green-naghdi model with the enhanced dispersive property. Journal of Computational Physics, 399:108953, 2019.

[48] YS Li, S-X Liu, Y-X Yu, and G-Z Lai. Numerical modeling of boussinesq equations by finite element method. Coastal Engineering, 37(2):97–122, 1999.

[49] Yeh H. Synolakis C. Liu, P.L.-F. Advanced numerical models for simulating tsunami waves and runup. Adv. Coast. Ocean Engng., 10, 2008.

[50] Per A Madsen and Ole R Sørensen. A new form of the boussinesq equations with improved linear dispersion characteristics. part 2. a slowly-varying bathymetry. Coastal engineering, 18(3-4):183–204, 1992.

[51] Fabien Marche. Combined hybridizable discontinuous galerkin (hdg)and runge-kutta discontinuous galerkin (rk-dg)formulations for green-naghdi equations onunstructured meshes. https://hal.archives-ouvertes.fr/hal-02319037v2.

[52] K.A. Mardal, X.-C. Tai, and R. Winther. A robust finite element method for darcy–stokes flow. SIAM J.Numer.Anal., 40(5):1605–1632, 2002.

[53] Amadine Menasaria. Accurate and efficient models for the simulation of wall bounded flows. PhD thesis, Arts et Métiers Paris Tech-Centre de Paris, 2019.

45

[54] Christopher Michalak and Carl Ollivier-Gooch. Accuracy preserving limiter for the high-order accurate solution of the euler equations. Journal of Computational Physics, 228(23):8693–8711, 2009.

[55] Dimitrios Mitsotakis, Boaz Ilan, and Denys Dutykh. On the galerkin/finite-element method for the serre equations. Journal of Scientific Computing, 61(1):166–195, 2014.

[56] Okey Nwogu. Alternative form of boussinesq equations for nearshore wave propagation. Journal of waterway, port, coastal, and ocean engineering, 119(6):618–638, 1993.

[57] Carl F. Ollivier-Gooch. Quasi-eno schemes for unstructured meshes based on unlimited data-dependent least-squares reconstruction. Journal of Computational Physics, 133(1):6–17, 1997.

[58] Hyoungsu Park, Daniel T Cox, Patrick J Lynett, Dane M Wiebe, and Sungwon Shin. Tsunami inundation modeling in constructed environments: A physical and numerical comparison of free-surface elevation, velocity, and momentum flux. Coastal Engineering, 79:9–21, 2013.

[59] D Howell Peregrine. Long waves on a beach. Journal of fluid mechanics, 27(4):815–827, 1967.

[60] Grégoire Pont, Pierre Brenner, Paola Cinnella, Bruno Maugars, and Jean-Christophe Robinet. Multiple-correction hybrid k-exact schemes for high-order compressible rans-les simulations on fully unstructured grids. Journal of Computational Physics, 350:45–83, 2017.

[61] Stéphane Popinet. A quadtree-adaptive multigrid solver for the serre–green–naghdi equations. Journal of Computational Physics, 302:336–358, 2015.

[62] M. Ricchiuto. An explicit residual based approach for shallow water flows. Journal of Computational Physics, 280:306–344, 2015.

[63] Mario Ricchiuto and Andreas Bollermann. Stabilized residual distribution for shallow water simulations. Journal of Computational Physics, 228(4):1071–1115, 2009.

[64] Mario Ricchiuto and Andrea Gilberto Filippini. Upwind residual discretization of enhanced boussinesq equations for wave propagation over complex bathymetries. Journal of Computational Physics, 271:306–341, 2014.

[65] P.J. Roache. Code Verification by the Method of Manufactured Solutions . Journal of Fluids Engineering, 124(1):4–10, 11 2001.

[66] Philip L Roe. Approximate riemann solvers, parameter vectors, and difference schemes. Journal of computational physics, 43(2):357–372, 1981.

[67] Florian Setzwein, Peter Ess, and Peter Gerlinger. High-order k-exact finite volume scheme for vertex-centered unstructured grids. In AIAA Scitech 2020 Forum, page 1785, 2020.

[68] Florian Setzwein, Moritz Spraul, Peter Ess, and Peter M Gerlinger. On the structure of correction matrices for a k-exact high-order finite-volume scheme on vertex-centered unstructured grids. In AIAA Scitech 2021 Forum, page 1548, 2021.

[69] Fengyan Shi, James T Kirby, Jeffrey C Harris, Joseph D Geiman, and Stephan T Grilli. A high-order adaptive time-stepping tvd solver for boussinesq modeling of breaking waves and coastal inundation. Ocean Modelling, 43:36–51, 2012.

[70] Mara Tonelli and Marco Petti. Hybrid finite volume–finite difference scheme for 2dh improved boussinesq equations. Coastal Engineering, 56(5):609–620, 2009.

[71] Davide Torlo and Ricchiuto Mario. Model order reduction strategies for weakly dispersive waves. submitted to Applied Mathematical Modelling,.

[72] Mark Walkley and Martin Berzins. A finite element method for the two-dimensional extended boussinesq equations. International Journal for Numerical Methods in Fluids, 39(10):865–885, 2002.

[73] Qian Wang, Yu-Xin Ren, and Wanai Li. Compact high order finite volume method on unstructured grids ii: extension to two-dimensional euler equations. Journal of Computational Physics, 314:883–908, 2016.

[74] Qian Wang, Yu-Xin Ren, Jianhua Pan, and Wanai Li. Compact high order finite volume method on unstructured grids iii: Variational reconstruction. Journal of Computational physics, 337:1–26, 2017.

[75] Z.J. Wang. Spectral (finite) volume method for conservation laws on unstructured grids. basic formulation: Basic formulation. Journal of Computational Physics, 178(1):210–251, 2002.

[76] Ge Wei and James T Kirby. Time-dependent numerical code for extended boussinesq equations. Journal of Waterway, Port, Coastal, and Ocean Engineering, 121(5):251–261, 1995.

[77] Ge Wei, James T Kirby, Stephan T Grilli, and Ravishankar Subramanya. A fully nonlinear boussinesq model for surface waves. part 1. highly nonlinear unsteady waves. Journal of Fluid Mechanics, 294:71–92, 1995.

[78] Robert W Whalin. The limit of applicability of linear wave refraction theory in a convergence zone. Technical report, Army Engineer Waterways Experiment Station Vicksburg Miss, 1971.

[79] Yao Zhang, Andrew B Kennedy, Tori Tomiczek, Aaron Donahue, and Joannes J Westerink. Validation of boussinesq–green–naghdi modeling for surf zone hydrodynamics. Ocean Engineering, 111:299–309, 2016.

[80] Yu-Si Zhang, Yu-Xin Ren, and Qian Wang. Compact high order finite volume method on unstructured grids iv: Explicit multi-step reconstruction schemes on compact stencil. Journal of Computational Physics, 396:161–192, 2019.
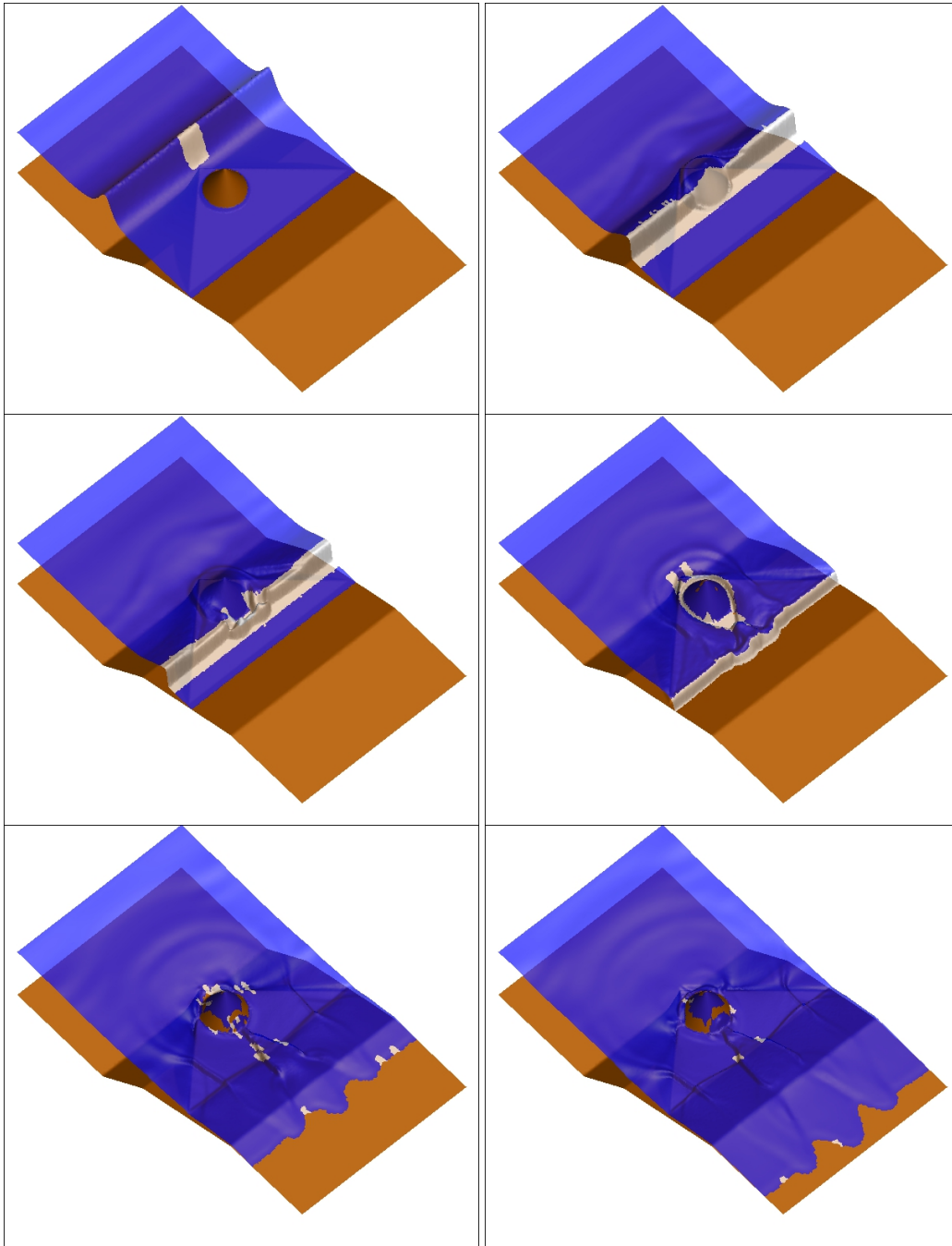
Figure 24: Solitary wave propagation over a three dimensional reef: evolution of fee surface solution. The white area represents the region where wave breaking is detected and the NLSW equations are solved.
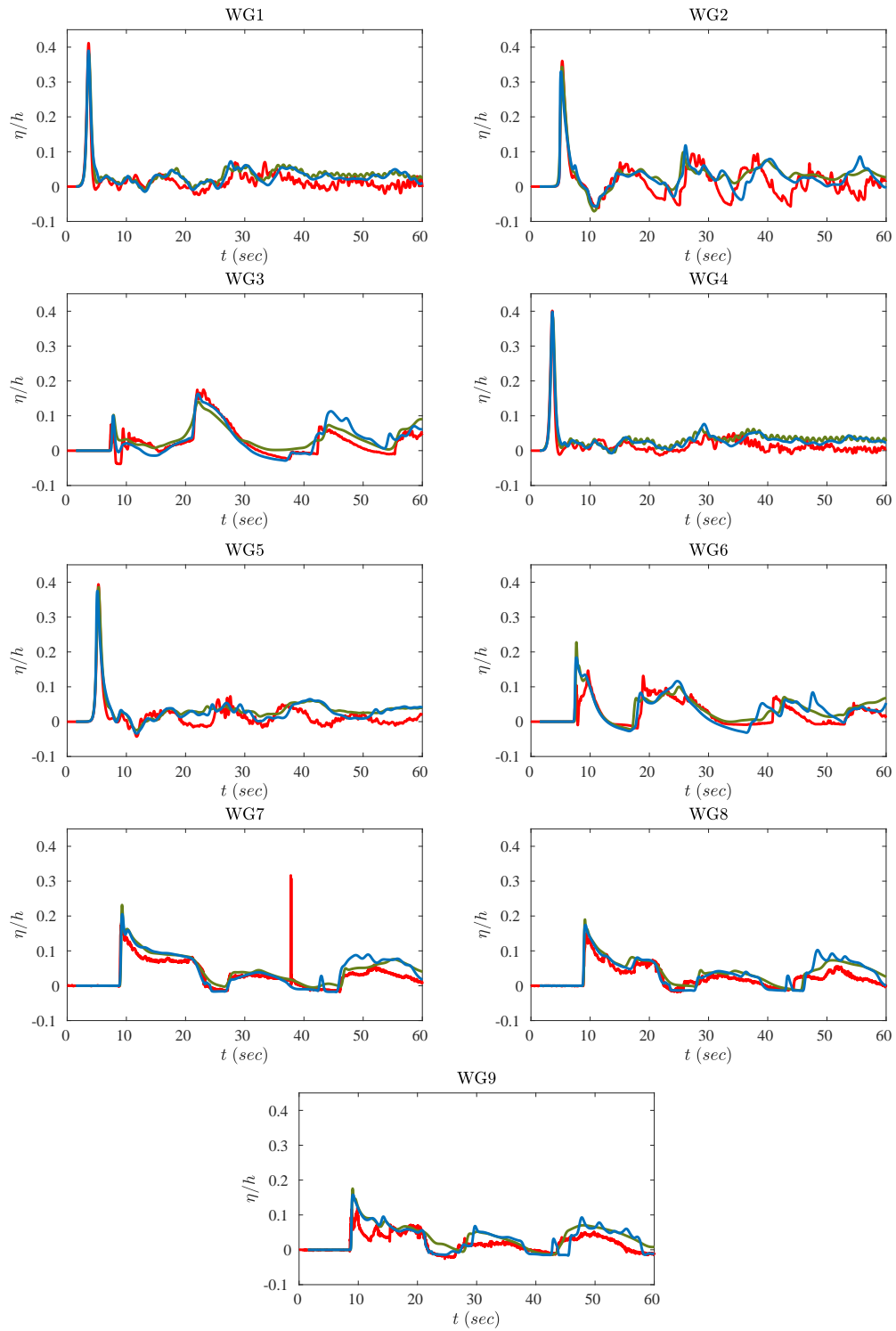
Figure 25: Solitary wave propagation over a three dimensional reef: computed time series of the free surface elevation on gauges positions

50
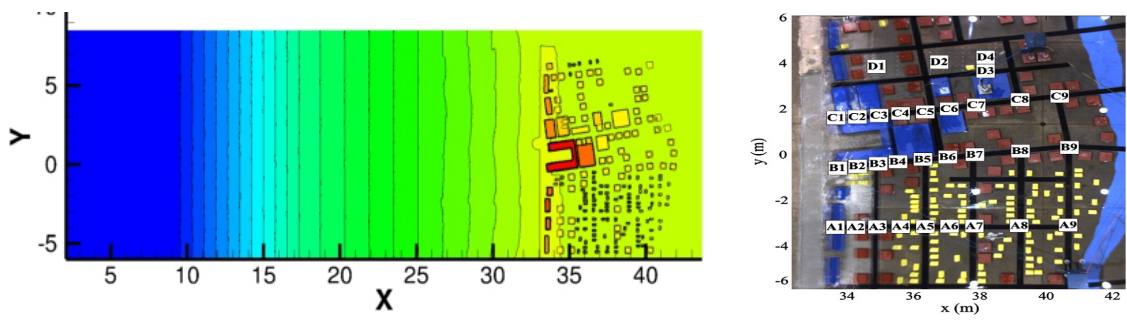
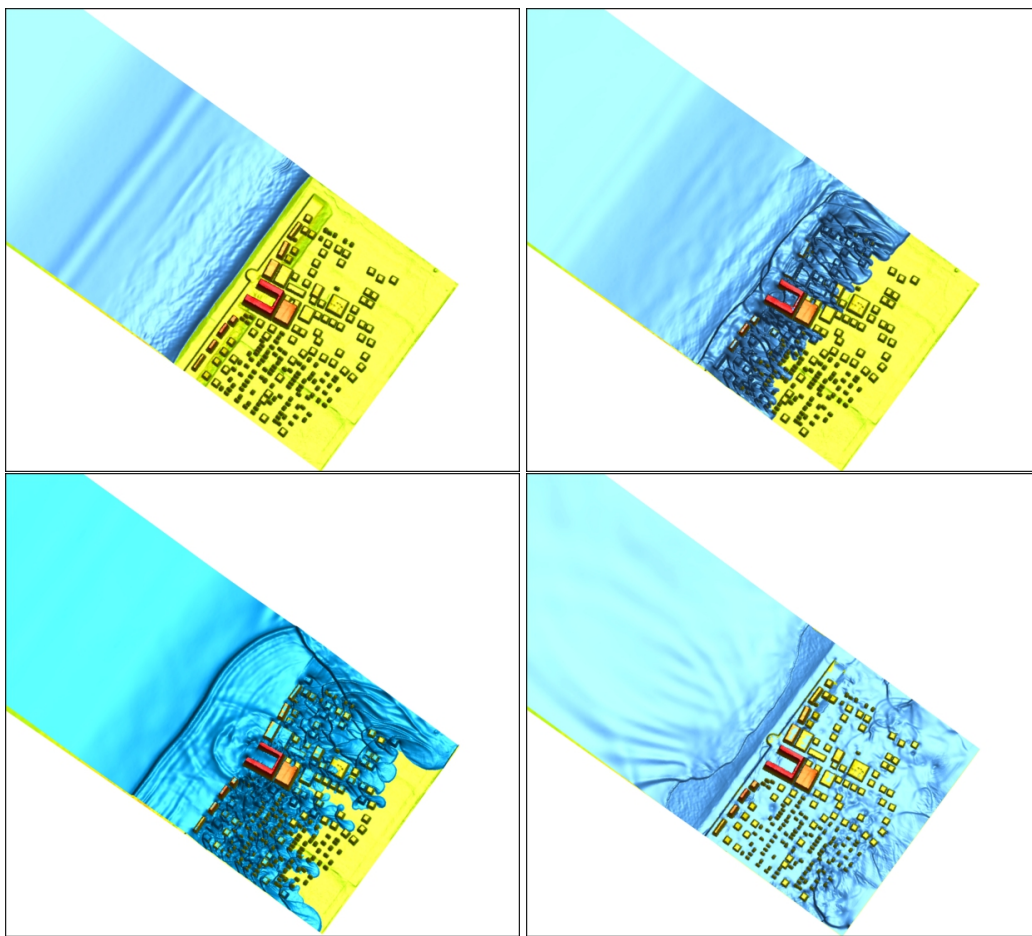Figure 26: Left: Contour lines of the topography. Right: Measurement locations. Picture taken form [58]

Figure 27: 3D view snapshots of the evolution of the wave after 14sec.

51
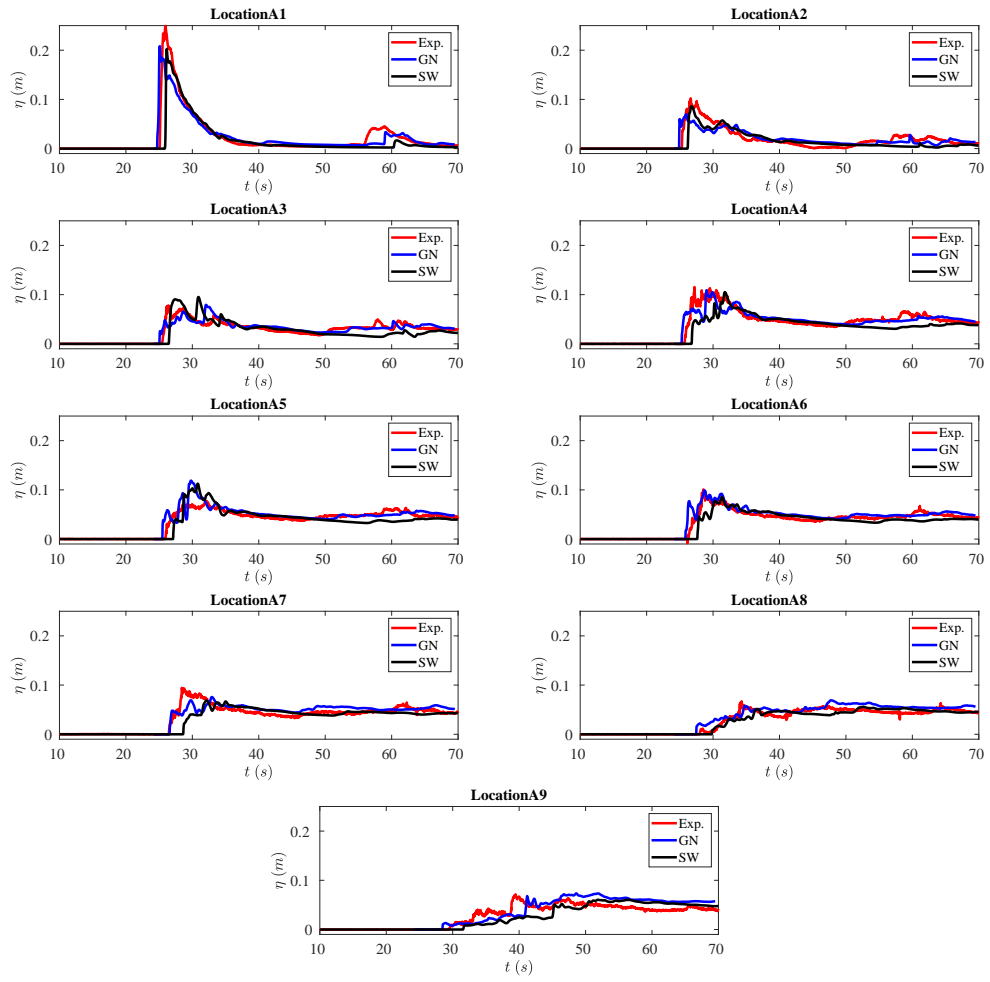
Figure 28: Free surface elevation measured in locations A
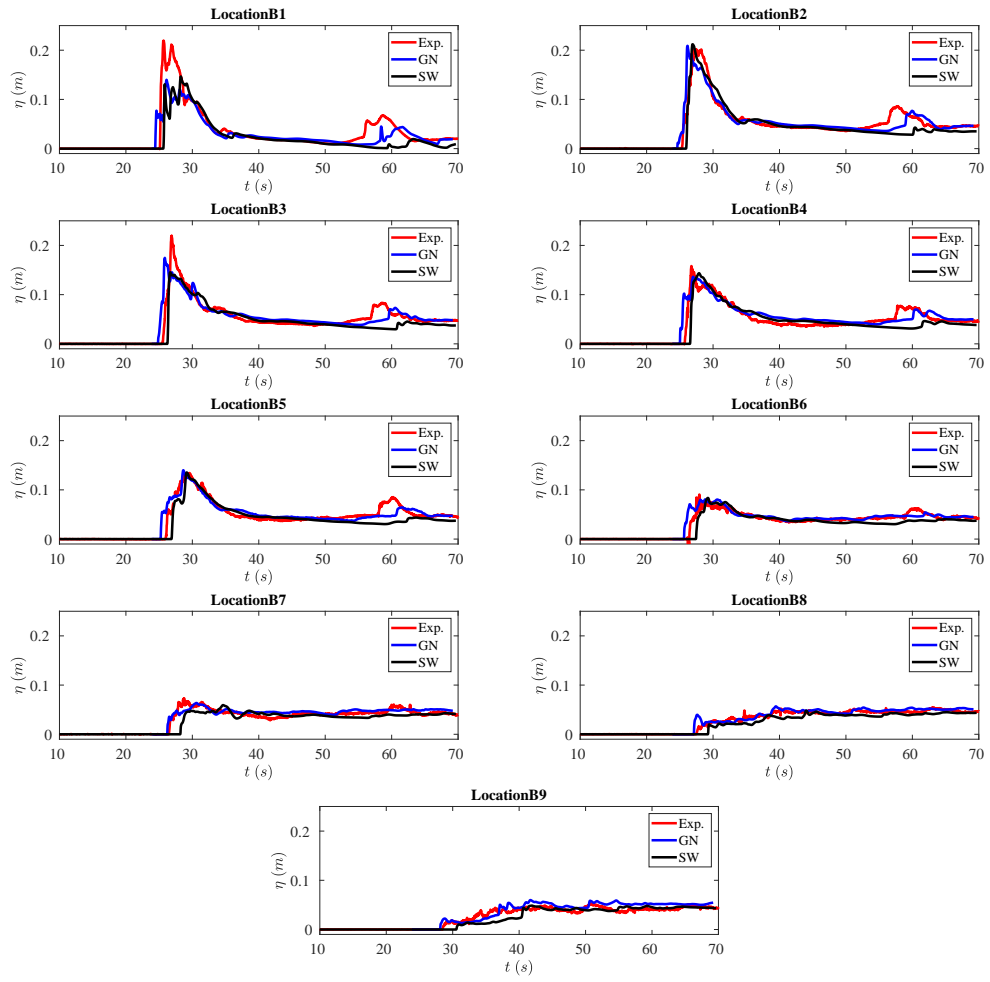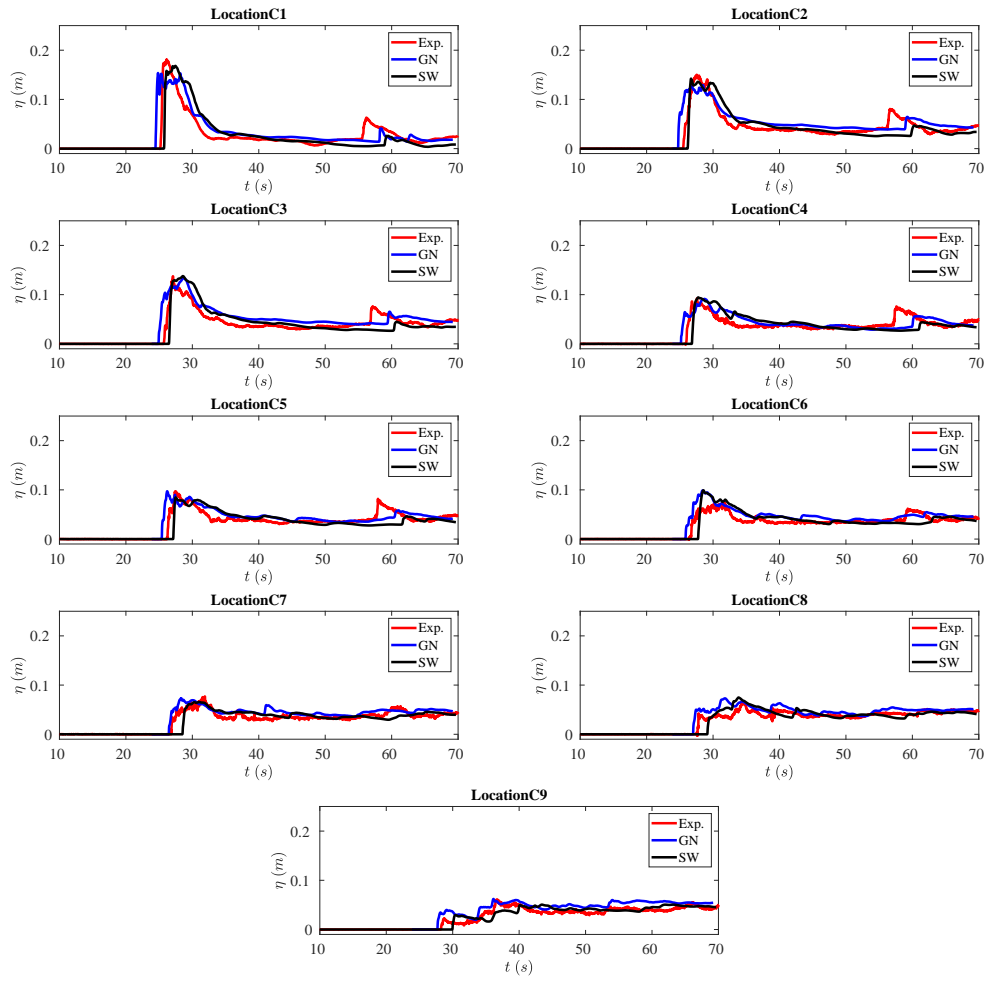
Figure 29: Free surface elevation measured in locations B

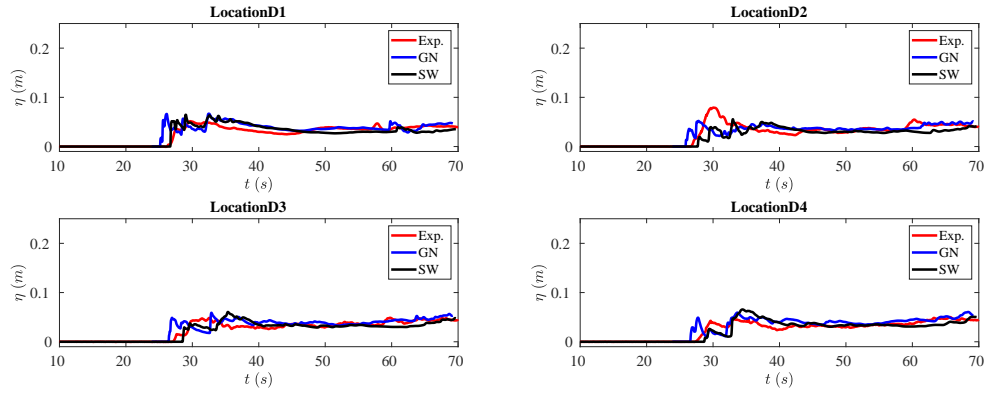Figure 30: Free surface elevation measured in locations C

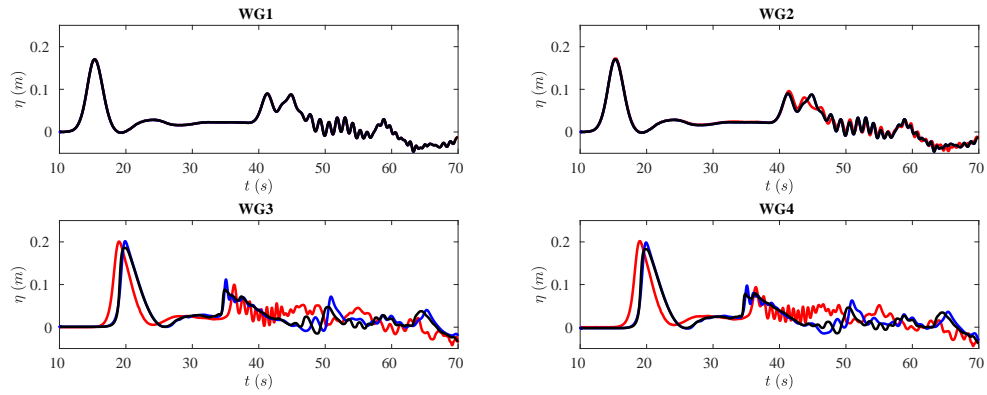Figure 31: Free surface elevation measured in locations D

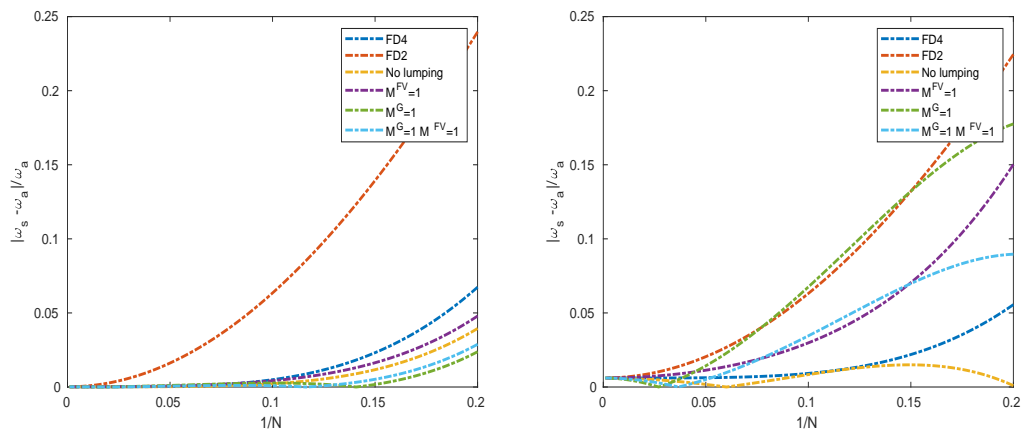Figure 32: Free surface elevation measured in wave gauges 1-4

Figure B.33: Dispersion error for FV with respect to ω_{airy}. $kh = 0.5$ and 2.5: impact of lumping strategy